18th AIAA/CEAS Aeroacoustics Conference (33rd AIAA Aeroacoustics Conference)
04 - 06 June 2012, Colorado Springs, CO

AIAA 2012-2158

Modeling of Noise Reduction for Turbulent Jets with Induced Asymmetry

Dimitri Papamoschou* and Sara Rostamimonjezi †
University of California, Irvine, Irvine, CA, 92697, USA

We present an acoustic analogy model for the noise reduction of dual-stream jets with induced asymmetry in the plume flow field, with emphasis on the direction of peak emission. The asymmetry redistributes the mean velocity and turbulent kinetic energy so that the underside of the jet becomes quiet. The goal of the model is to predict the change in acoustics, relative to a known baseline, due to the redistribution of the mean flow as computed by a Reynolds-Averaged Navier Stokes (RANS) solver. It is assumed that the changes in the flow field are moderate enough that the non-dimensional parameters governing the source space-time correlation are the same in the baseline (symmetric) and deformed (asymmetric) jets. Those parameters are determined by minimizing the difference between modeled and experimental far-field spectra of the baseline jet using the conjugate gradient method. A generalized form of the space-time correlation allows shapes beyond the traditional exponential forms. This flexibility enables a very good match between the modeled and experimental spectra. The resulting non-dimensional parameters are then used to compute the spectra of the asymmetric jets. Included in the formulation of the acoustic analogy model is an azimuthal directivity based on the wavepacket model of large-scale-structure noise. The predicted noise reduction is in reasonable agreement with the experiments. The study underscores the importance of a properly defined convective Mach number, based on the RANS solution, for modeling large-scale-structure noise.

Nomenclature

a	=	speed of sound
A	=	cross sectional area; amplitude
C	=	correlation coefficient
H	=	wavenumber-frequency spectrum
k	=	turbulent kinetic energy
k_x	=	axial wavenumber
K	=	transformed lateral wavenumber
L	=	characteristic length scale
M	=	Mach number
M_c	=	convective Mach number
r	=	distance between source and observer
R	=	observer distance in spherical coordinate system; correlation function
p	=	static pressure
T	=	Lighthill stress tensor
u, v, w	=	velocities in Cartesian coordinate system
u_*	=	characteristic velocity scale
U	=	fully-expanded velocity
U_c	=	convective velocity
x, Y, z	=	Cartesian coordinate system
y	=	radial coordinate
U_c	=	convective velocity

*Professor, Department of Mechanical and Aerospace Engineering, Fellow AIAA
†Graduate Student Researcher, Department of Mechanical Aerospace Engineering, Member AIAA

α	=	acoustic wavenumber = ω/a_∞
$\boldsymbol{\alpha}$	=	wavenumber vector in direction of observer = $\alpha\mathbf{x}/R$
β	=	shape parameter
γ	=	specific heat ratio
Γ	=	azimuthal influence function
ϵ	=	dissipation
θ	=	polar angle relative to jet axis
ϑ	=	direction cosine
ϕ	=	azimuthal angle relative to downward vertical
φ	=	acoustic potential
ρ	=	density
ω	=	angular frequency
Ω	=	specific dissipation = ϵ/k

Subscripts

i, j, k, l	=	correlation indices
p	=	primary (core) exhaust
s	=	secondary (bypass) exhaust
v	=	condition at axial location of vanes
∞	=	ambient (flight) conditions

I. Introduction

The exhaust of jet engines continues to be a significant contributor to airport noise. The problem is particularly acute for low-bypass, high-performance turbofan engines that are envisioned to power the next generation of supersonic transports. Even for large-bypass ratio engine powering subsonic commercial aircraft, jet noise remains a problem and an area of active research.

In the last couple of decades, the bulk of the jet noise suppression effort has focused on chevrons, a sawtooth pattern on the trailing edge of exhaust nozzles. Recently, methods to reduce noise by inducing asymmetry of the exhaust plume have received some attention.[1] One of these concepts is the fan flow deflection (FFD) method wherein a redistribution of the fan exhaust suppresses noise from the core stream directed towards the ground. The general concept of FFD is illustrated in Fig. 1. The redistribution of the fan stream can be achieved with vanes internal to the fan duct or a wedge-shaped deflector placed outside the fan nozzle. These devices act as force generators to concentrate the fan stream in the sideward and downward directions relative to the core jet, thus elongating the secondary core (SC, defined by the inflection points i_2 and i_3), relative to the primary core (PC), in those directions. The elongation of the secondary core has two effects, the reduction in velocity gradients in the primary shear layer (and attendant reduction in turbulence production) and reduction of the convective Mach number of the primary shear layer.[2] Recent modeling efforts for the overall sound pressure level have focused on the reduction in the turbulent kinetic energy.[3] However, we expect the reduction in convective Mach number to play an important role as well, particularly in high-speed jets with intense Mach wave radiation.

Development of the FFD and similar methods will be facilitated by an engineering design tool that predicts the noise *reduction* from a known baseline, based on the time-averaged first- and second-order statistics generated by of Reynolds Averaged Navier Stokes (RANS) solvers. In our past work we constructed preliminary correlations of the change in overall sound pressure level (OASPL) with the change in peak turbulent kinetic energy.[3] We now extend those studies to predicting the change of the sound pressure level (SPL) spectrum as a result of the asymmetry induced in the flow. The first step is the development of an acoustic analogy model that gives a reasonable representation of the SPL spectrum for the baseline (symmetric) jet. Although we do not seek to predict the spectrum of the baseline jet per se (we assume that is is known), we calibrate the model such that it matches the baseline SPL spectrum. This gives confidence that the model has the proper distributions for the space-time correlation of the noise source term. Then the model is used to predict the change in SPL as a result of the redistribution of the mean flow and its turbulent statistics. The focus of this paper is on the peak noise emission of the jet which is caused by large-scale turbulent structures.

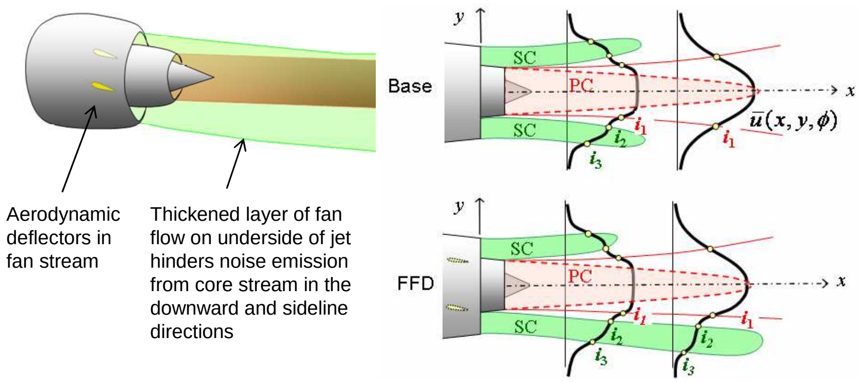

Figure 1. Fan flow deflection method for jet noise reduction. Schematics illustrate the elongation of the secondary core with application of the deflection.

Our work is influenced by the large body of work on acoustic analogy, starting with Lighthill[4] and including Morris and Farrasat,[5] Harper-Bourne[6] and many others cited in following sections. To maintain the simplicity of the acoustic analogy based on the Lighthill equation, our modeling does not include explicitly effects of refraction which would have required more complex approaches like Lilley's equation[7] or Linear Euler Equation (LEE) solvers.[8,9] In past works refraction has been approached from the standpoint of localized sources embedded in a mean flow.[10,11] This concept is questionable as far as *outward* radiation from large-scale, coherent structures is concerned. The large-scale structures do not "know" that a mean shear flow exists - in fact they create the mean shear in a time-averaged sense. There is no physical reason to expect that the shear profile created by the structures (again, in a mean sense) should impact significantly their acoustic emission. Regarding *inward* radiation into the potential core, and refraction/reflection from the other side of the jet, we will present elementary arguments that this radiation is very weak because a disturbance that is intrinsically supersonic (radiative) with respect to the ambient must be intrinsically subsonic (decaying) with respect to the jet flow for typical aeroengine operating conditions. In this study the azimuthal directivity of asymmetric jets is handled by connecting the "source" of the acoustic analogy formulation to a stochastic wavepacket model for the large-scale noise.

The paper has the following organization. Section II reviews the basic steps of the Lighthill acoustic analogy and implements a model for the cross-correlation that allows a larger range of functions than previously used. Section III makes a preliminary connection between the acoustic analogy model and the wavepacket model of large scale structure noise; this connection is used to establish an azimuthal directivity in the acoustic analogy model. Section IV describes the parameterization of the source whereby the coefficients of various scales are determined for the baseline axisymmetric jet. Section V outlines the experimental sound measurements and the computational RANS predictions for the jets. Section VI presents the results of the acoustic analogy model with application to the jets with fan flow deflection. Section VII reviews key assumptions related to the use of the wavepacket model. The paper concludes with Section VIII.

II. Acoustic Analogy Model

A. Fundamental Relations

Here we review briefly the background of the Lighthill acoustic analogy,[12] emphasizing features that are salient to the modeling effort of this study. Referring to Fig. 2, the noise source region has a volume $\mathcal{V}$, location $\mathbf{y}$ refers to a point inside the source region, location $\mathbf{x}$ is the observer location outside the source region, and $r = |\mathbf{x} - \mathbf{y}|$ is the distance between source and observer. Through a rearrangement of the Navier-Stokes equations, the pressure fluctuation p' outside the source region can be shown to satisfy the linear inhomogeneous wave equation

$$\frac{1}{a_\infty^2}\frac{\partial^2 p'}{\partial t^2} - \frac{\partial^2 p'}{\partial x_i \partial x_i} = \frac{\partial^2 T_{ij}}{\partial x_i \partial x_j} \tag{1}$$

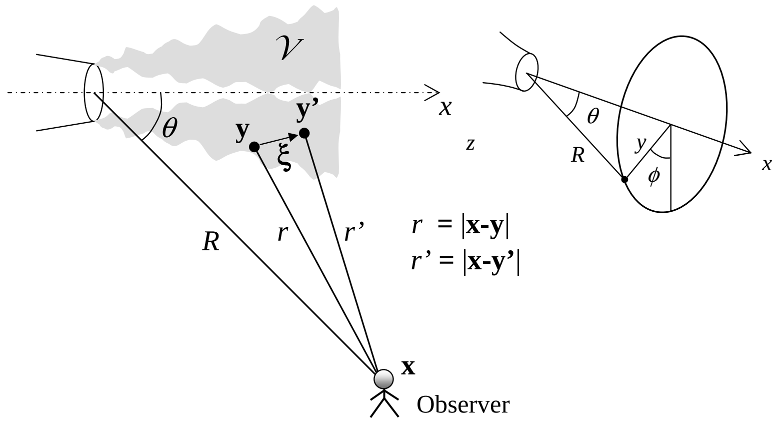

Figure 2. Nomenclature and coordinate system for acoustic analogy model.

where a_∞ is the speed of sound of the uniform stationary medium surrounding the source and T_{ij} is the Lighthill stress tensor

$$T_{ij} = \rho u_i u_j + (p' - a_\infty^2 \rho')\delta_{ij} - \tau_{ij} \tag{2}$$

The exact solution to Eq. 1 is

$$p'(\mathbf{x},t) = \frac{1}{4\pi}\frac{\partial^2}{\partial x_i \partial x_j}\int_{\mathcal{V}} T_{ij}\left(\mathbf{y}, t - r/a_\infty\right)\frac{1}{r}d^3\mathbf{y} \tag{3}$$

Applying the chain rule, and neglecting terms that decay faster than the inverse first power of the distance, the double divergence is converted to double time derivative,

$$p'(\mathbf{x},t) = \frac{1}{4\pi a_\infty^2}\int_{\mathcal{V}} \vartheta_i \vartheta_j \frac{\partial^2 T_{ij}}{\partial t^2}\left(\mathbf{y}, t - r/a_\infty\right)\frac{1}{r}d^3\mathbf{y} \tag{4}$$

where

$$\vartheta_i \;=\; \frac{x_i - y_i}{r} \tag{5}$$

is the direction cosine between observer and source. Even though the derivative transformation in Eq. 4 is commonly associated with a far-field approximation, it is important to note that Eq. 4 gives the *acoustic* pressure everywhere, that is, in the near field and in the far field.[12–14] This is because the neglected terms in the transformation decay faster than r^{-1} and thus comprise the hydrodynamic pressure. Taking the Fourier transform of Eq. 4, we relate the Fourier transform of the pressure, $P(\mathbf{x},\omega)$, to the Fourier transform of the Lighhill tensor, $Q_{ij}(\mathbf{x},\omega)$:

$$P(\mathbf{x},\omega) = \frac{\omega^2}{4\pi a_\infty^2}\int_{\mathcal{V}} \vartheta_i \vartheta_j Q_{ij}(\mathbf{y},\omega)\frac{e^{-i\omega r/a_\infty}}{r}d^3\mathbf{y} \tag{6}$$

Equation 6 is the basis for obtaining the autospectrum of the acoustic pressure. Multiplying times the complex conjugate and time-averaging (operation: <>),

$$< P^*(\mathbf{x},\omega)P(\mathbf{x},\omega) >= \frac{\omega^4}{16\pi^2 a_\infty^4}\int_{\mathcal{V}}\int_{\mathcal{V}'} \vartheta_i \vartheta_j \vartheta'_k \vartheta'_l < Q^*_{ij}(\mathbf{y},\omega)Q_{kl}(\mathbf{y}',\omega) > \frac{e^{i\alpha(r-r')}}{rr'}d^3\mathbf{y}d^3\mathbf{y}' \tag{7}$$

where $\alpha = \omega/a_\infty$ is the acoustic wavenumber and $\vartheta'_i = (x_i - y'_i)/r'$. The left hand side is the pressure autospectrum $S_{pp}(\mathbf{x},\omega)$. Letting $\boldsymbol{\xi} = \mathbf{y}' - \mathbf{y}$ denote the separation vector between two source elements, we relate the source cross-spectrum to the space-time correlation:

$$< Q^*_{ij}(\mathbf{y},\omega)Q_{kl}(\mathbf{y}',\omega) > = \int_{-\infty}^{\infty} R_{ijkl}(\mathbf{y},\boldsymbol{\xi},\tau)e^{-i\omega\tau}d\tau \tag{8}$$

and the equation for the autospectrum becomes

$$S_{PP}(\mathbf{x},\omega) = \frac{\omega^4}{16\pi^2 a_\infty^4}\int_{\mathcal{V}}\int_{\mathcal{V}_\xi}\int_{-\infty}^{\infty}\vartheta_i\vartheta_j\vartheta'_k\vartheta'_l\ R_{ijkl}(\mathbf{y},\boldsymbol{\xi},\tau)\frac{\exp\left[i(\alpha(r-r')-\omega\tau)\right]}{rr'}d\tau d^3\boldsymbol{\xi} d^3\mathbf{y} \tag{9}$$

with $r = |\mathbf{x}-\mathbf{y}|$ and $r' = |\mathbf{x}-\mathbf{y}-\boldsymbol{\xi}|$. Equation 9 gives the acoustic component of the pressure field everywhere. At this point the only assumption is the stationarity of the turbulent statistics.

When the observer is in the geometric far field, several approximations simplify Eq. 9. First, $r' \approx r \approx R$. Second, we calculate with the aid of Fig. 2 that

$$\alpha(r-r') \ \approx\ \boldsymbol{\alpha}\cdot\boldsymbol{\xi} \tag{10}$$

where $\boldsymbol{\alpha} = \alpha\mathbf{x}/R$ is the wavenumber vector in the direction of the observer. Finally, the directions cosines are referenced to the origin, $\vartheta_i = \vartheta'_i = x_i/r$, and operate on R_{ijkl} to give its component R_{xxxx} in the direction of the observer. On defining the wavenumber-frequency spectrum as

$$H(\mathbf{y},\boldsymbol{\alpha},\omega) \ =\ \int_{\mathcal{V}_\xi}\int_{-\infty}^{\infty} R_{xxxx}(\mathbf{y},\boldsymbol{\xi},\tau)\exp\left[i(\boldsymbol{\alpha}\cdot\boldsymbol{\xi}-\omega\tau)\right]d\tau\ d^3\boldsymbol{\xi} \tag{11}$$

the pressure autospectrum in the geometric far field becomes

$$S_{PP}(\mathbf{x},\omega) = \frac{\omega^4}{16\pi^2 a_\infty^4 R^2}\int_{\mathcal{V}} H\left(\mathbf{y},\boldsymbol{\alpha},\omega\right)d^3\mathbf{y} \tag{12}$$

B. Model for Space-Time Correlation

At the heart of acoustic analogy modeling is the assumed form of the two-point correlation $R_{ijkl}(\mathbf{y},\boldsymbol{\xi},\tau)$ in Eqs. 9 or 11. There is a large variety of models proposed in the past, perhaps the more physical being the model of Bassetti et al.[15] However, the non-separable nature of their model requires a 4D Fourier transform, a very expensive operation that renders the model impractical for the present investigation because the model must be evaluated hundreds of times to optimize the solution. Among the separable models, the Tam-Auriault formulation[16] has found wide use for predicting both fine-scale noise[16] and large-scale noise.[17] Here we use a generalization of the Tam-Auriault model wherein the shape of the various correlation functions is flexible. The separation $\boldsymbol{\xi}$ is expressed in polar-spherical coordinates as $\boldsymbol{\xi} = (\xi_x,\xi_y,\xi_\phi)$. The correlation has the form

$$R_{ijkl}(\mathbf{y},\boldsymbol{\xi},\tau) \ = A_{ijkl}(\mathbf{y})\ R_1\left(\frac{\xi_x}{L_\tau(\mathbf{y})}\right)R_2\left(\frac{\xi_y}{L_y(\mathbf{y})}\right)R_3\left(\frac{\xi_\phi}{L_\phi(\mathbf{y})}\right)R_4\left(\frac{\xi_x-\widetilde{u}\tau}{L_x(\mathbf{y})}\right) \tag{13}$$

Here $A_{ijkl}(\mathbf{y})$ is the amplitude of the correlation and has units of $\rho^2 u^4$; $R_1 \ldots R_4$ are correlation functions; L_x, L_y, and L_ϕ are correlations length scales in the axial, radial and circumferential (azimuthal) directions, respectively; L_τ is a length scale that depends on the turbulent time scale τ_*; and $\widetilde{u}$ is a characteristic velocity associated with the convection of the mean flow or the convection of the turbulent eddies.

In the geometric far field the wavenumber vector in the direction of the observer has the components

$$\boldsymbol{\alpha} \ =\ \alpha(\cos\theta,\ \sin\theta,\ 0) \tag{14}$$

thus

$$\boldsymbol{\alpha}\cdot\boldsymbol{\xi} = \alpha(\xi_x\cos\theta,\ \xi_y\sin\theta,\ 0) \tag{15}$$

Further, we denote $A_{xxxx} = \vartheta_i\vartheta_j\vartheta'_k\vartheta'_l A_{ijkl}$. Applying the Fourier transforms of Eq. 11,

$$H(\mathbf{y},\boldsymbol{\alpha},\omega) \ =\ A_{xxxx}L_\tau L_y L_\phi\frac{L_x}{\widetilde{u}}\ \widehat{R}_1\left(\alpha L_\tau\frac{\widetilde{u}\cos\theta - a_\infty}{\widetilde{u}}\right)\ \widehat{R}_2\left(\alpha L_y\sin\theta\right)\ \widehat{R}_3(0)\ \widehat{R}_4\left(\frac{\omega L_x}{\widetilde{u}}\right) \tag{16}$$

We may elect $\widetilde{u}$ to be the mean flow velocity or the convection velocity of the turbulent eddies. The two velocities can be very different. In this study we set $\widetilde{u} = U_c$ where U_c is the convection velocity of the large-scale structures which will be topic of further discussion. This selection is consistent with the focus of our work on modeling the noise reduction in the direction of peak emission. Then the convective Mach number $M_c = u_*/a_\infty = U_c/a_\infty$ represents the Mach number of large-scale structures (instability waves) with respect to the ambient medium. On selecting $L_\tau = U_c\tau_*$, Eq. 16 takes the form

$$H(\mathbf{y},\boldsymbol{\alpha},\omega) \;=\; A_{xxxx}\;\tau_* L_x L_y L_\phi\;\widehat{R}_1\left[\omega\tau_*(M_c\cos\theta-1)\right]\;\widehat{R}_2\left(\alpha L_y\sin\theta\right)\;\widehat{R}_3(0)\;\widehat{R}_4\left(\frac{\alpha L_x}{M_c}\right) \tag{17}$$

The generic correlation function is selected as

$$R(t,\beta) \;=\; e^{-|t|^\beta} \tag{18}$$

which is sometimes called the stretched exponential for $0<\beta<1$ and the compressed exponential for $\beta>1$.[18] Thus $R_j(t) = R(t,\beta_j)$. Since R is an even function, its Fourier transform is twice the cosine transform:

$$\widehat{R}(\eta,\beta) \;=\; 2\int_0^\infty R(t,\beta)\cos(\eta t)dt \tag{19}$$

The wavenumber-frequency spectrum can then be expressed as

$$H(\mathbf{y},\boldsymbol{\alpha},\omega) \;=\; A_{xxxx}\;\tau_* L_x L_y L_\phi\;\widehat{R}\left(\omega\tau_*(M_c\cos\theta-1),\beta_1\right)\;\widehat{R}\left(\alpha L_y\sin\theta,\beta_2\right)\;\widehat{R}(0,\beta_3)\;\widehat{R}\left(\frac{\alpha L_x}{M_c},\beta_4\right) \tag{20}$$

Note that $\widehat{R}$ assumes the forms

$$\widehat{R}(\eta,1) \;=\; \frac{2}{1+\eta^2}$$
$$\widehat{R}(\eta,2) \;=\; \sqrt{\pi}e^{-\frac{1}{4}\eta^2}$$

For powers β other than 1 (exponential) or 2 (Gaussian) the Fourier transform does not have an analytical expression and needs to be calculated numerically. For computational efficiency, the transform $\widehat{R}(\eta,\beta)$ was computed once and was tabulated; subsequent operations used 2D interpolation of the table. Figure 3 illustrates the behavior of the stretched/compressed exponential and its transform for $0.7\le\beta\le 2$, the range allowed in this study. For clarity the transform is shown in decibels.

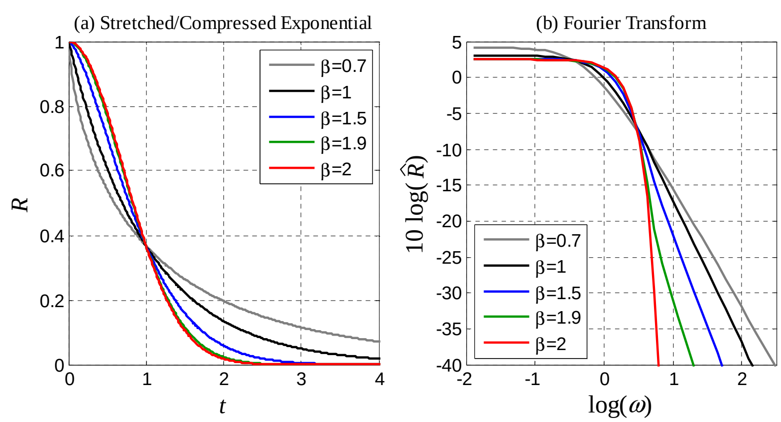

Figure 3. Correlation function (a) and its Fourier transformation (b) for various values of β.

C. Characteristic Scales

The length, time, and velocity scales of the correlations are based on RANS predictions of the flow field, to be presented in Section IV. The RANS simulation generates the mean velocity field $\overline{\mathbf{u}} = (\overline{u},\overline{u},\overline{w})$ (Cartesian coordinates), the density field $\overline{\rho}$, the turbulent kinetic energy k and the dissipation ϵ. The specific dissipation is defined as $\Omega = k/\epsilon$ and has units of frequency. Below we present the classical constructions of length, time, and velocity scales for acoustic analogy modeling.

$$
\begin{aligned}
L_x &= C_1 \frac{k^{3/2}}{\epsilon} = C_1 \frac{k^{1/2}}{\Omega} \\
L_y &= C_2 \frac{k^{3/2}}{\epsilon} = C_2 \frac{k^{1/2}}{\Omega} \\
L_\phi &= L_y \\
\tau_* &= C_4 \frac{k}{\epsilon} = C_4 \frac{1}{\Omega} \\
u_* &= \sqrt{\frac{2k}{3}}
\end{aligned}
\tag{21}
$$

Regarding the amplitude term A_{ijkl}, we assume that the principal component of the Lighthill stress tensor is $T_{ij} = \overline{\rho} u_i u_j$. With $u_1 = \overline{u} + u'$, $u_2 = v'$, and $u_3 = w'$ we examine the effects of the various terms on the cross-spectrum of Eq. 8 and arrive at the relation

$$
A_{ijkl} = \left\lfloor 2^{f_1 - 2} \right\rfloor \overline{\rho}^2 \, \overline{u}^2 u_*^2 + \overline{\rho}^2 u_*^4 \tag{22}
$$

Here f_1 is the frequency of index 1 in (i, j, k, l) and $\lfloor . \rfloor$ denotes the floor function (greatest integer less than or equal to the argument). The first term on the right-hand side represents the "shear noise" and the second term represents the "self noise." The construction of Eq. 22 follows the general lines of Ribner,[19] although it includes non-axisymmetric contributions that Ribner neglected. Even though Eq. 22 is basically a dimensional statement, the turbulence intensity measurements of Harper-Bourne[14] suggest that setting the second-order correlations equal to u_*^2 and the fourth-order correlations equal to u_*^4 may hold quantitatively as well.

In the far field, the amplitude reduces to

$$
A_{xxxx} = \overline{\rho}^2 \, \overline{u}^2 u_*^2 (\cos^4\theta + \cos^2\theta \sin^2\theta \sin^2\phi) + \overline{\rho}^2 u_*^4 \tag{23}
$$

as shown by Ribner.[19] For an axisymmetric jet the $\sin^2\phi$ term averages to $1/2$ and the coefficient of the shear-noise term becomes $(\cos^4\theta + \cos^2\theta)/2$. Having evaluated the impact of the $\sin^2\phi$ term on our asymmetric jets we found that its influence is too small to warrant complicating the analysis with its inclusion. Expecting the contribution of the self-noise term to be small in the direction of peak emission we set

$$
A_{xxxx} = B \, \overline{\rho}^2 \, \overline{u}^2 u_*^2 \tag{24}
$$

where B is a fitting constant that absorbs the cosine terms. We note that setting A_{xxxx} proportional to the self-noise term gave practically identical results in our parameterization scheme.

Much more crucial is the formulation of the convective Mach number M_c. As is evident in the $\widehat{R}_1$ term of the wavenumber-frequency spectrum (Eqs. 17, 20), the convective Mach number plays a vital role on the radiation efficiency, particularly when M_c is high subsonic or supersonic. When $M_c \cos\theta = 1$ a volume element radiates with 100% efficiency in the direction θ. Detailed hot-wire measurements of space-time correlations in a subsonic jet[20] indicate that the convective speed U_c varies with radial location, following the mean velocity $\overline{u}$ but with a smaller radial gradient than $\overline{u}$. It was thus suggested that setting $U_c = \overline{u}$ is a reasonable approximation. However, when dealing with large-scale "coherent" structures, that is, structures that span the integral length scale of the shear layer, the appropriateness of using $U_c = \overline{u}$ should be questioned, particularly in high-speed jets. First, eddies with $U_c = \overline{u}$ cannot emit Mach waves (they are intrinsically subsonic), which is contrary to the vast experimental evidence of Mach wave emission. Second, there is strong experimental evidence, starting from the seminal experiments of Brown and Roshko,[21] that coherent structures have one convective velocity over their lifetime.[22,23]

Because our work tries to model noise in the direction of peak emission, the choice $M_c = \overline{u}/a_\infty$ appears problematic for the reasons delineated above. It turns out that the RANS simulation provides guidance as to a better definition for M_c. As will be seen in Section IV, the Mach number $\overline{u}/a_\infty$ *at the locus of the peak turbulent kinetic energy* displays trends that capture the physical evolution of M_c in a dual-stream jet, and particularly the trends associated with the fan flow deflection illustrated in Fig. 1. The locus of peak k is a surface around the jet axis defined by the radial location $y_m(x, \phi)$ where k is maximized at given axial location x and azimuthal angle ϕ. Letting $\mathbf{y} = (x, y, \phi)$ represent the location of a volume element in polar coordinates (Fig. 2), the convective Mach number of that volume element is defined as

$$M_c(x, y, \phi) \;=\; \frac{\overline{u}(x, y_m(x, \phi), \phi)}{a_\infty} \tag{25}$$

This means that all the volume elements at a particular x and ϕ are assigned the same value of M_c corresponding to the local maximum of k. A similar definition for M_c was used by Karabasov et al[17] where the convection velocity was determined from the location of the maximum in the fourth-order velocity cross-correlation.

For a given polar angle, the far-field autospectrum is parameterized in terms of the scale coefficients C_1, C_2, C_4 and the shape coefficients $\beta_1, \beta_2, \beta_4$ that govern the correlation function, Eq. 13. As seen in Eq. 20 the coefficient β_3 (corresponding to the circumferential correlation) affects only the amplitude of the spectrum, in a very minor way, and therefore is not a critical parameter.

III. Azimuthal Directivity

In this study we are dealing with asymmetric jets whose source distribution has strong azimuthal variation. The acoustic analogy model formulated in Section II integrates over the entire volume of noise sources without accounting for directivity effects in the azimuthal direction. To formally account for such effects we need to include the elements of refraction as sound propagates from the shear layer through the mean flow of the jet and out into the ambient medium. This would entail a much more complex acoustic analogy model using Lilley's equation[7] or LEE approaches.[8] The computational cost of these approaches can be similar to or exceed the cost of the RANS solution. To address this issue while preserving the simplicity of

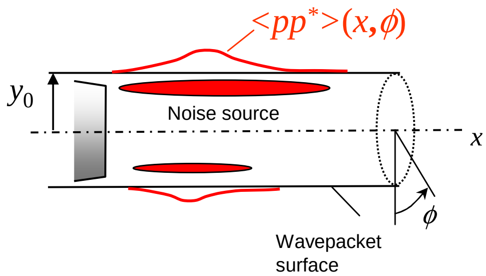

Figure 4. Wavepacket model and coordinate system.

the Lighthill acoustic analogy we invoke the wavepacket model of jet noise and attempt a link between the volumetric noise source in the Lighthill integral to a surface source that defines the wavepacket.

A. Wavepacket Model of Jet Noise

In its most general form, the wavepacket model is an application of Kirchhoff's surface integral.[24] We prescribe an acoustic field (pressure or acoustic potential) on a surface then propagate this field outward using the appropriate wave propagator. The prescribed field on the surface may represent the typical behavior of instability waves[25–30] or may be calculated from the volume sources enclosed by the surface.[31] The wavepacket model illustrated in Fig. 4 is based on the following assumptions:

- The wavepacket surface is taken to be close enough to the source region so that the "imprint" (pressure field) of the source on the surface has nearly the same azimuthal variation as the source itself. This assumes a thin annular region of the dominant sources in the jet, as illustrated in Fig. 4.
- The propagation of sound within the surface is sufficiently weak, due to refraction effects by the mean flow, that it can be neglected compared to the outward propagation of sound.

The validity of the above assumptions will be assessed by a simple 2D model of refraction through the jet flow and by application of the exact Lighthill solution, Eq. 9, to compute the pressure autospectrum on the wavepacket cylinder.

B. Surface Source Formulation

Suppose that we envelop the source region with a cylindrical surface of radius $y = y_0$ (Fig. 4). For given frequency ω (harmonic form $e^{-i\omega t}$) we envision the pressure field on the wavepacket surface consisting of random, uncorrelated events of the form

$$p(x,\phi) \; = \epsilon \; p_0 \left(\frac{x}{L_x}\right) \mathcal{D}\left(\frac{\phi-\phi'}{\Delta\phi}\right) \tag{26}$$

where ϵ is a random amplitude and ϕ' is a random azimuthal angle distributed in the interval $[-\pi,\pi]$ with probability density function $f(\phi')$. The concept of Eq. 26 was introduced at an elementary level in Ref. 30 and is further developed in Ref. 32. Each event can be visualized as a "bump" with random amplitude, random orientation, but deterministic axial and azimuthal shapes. The scales L_x and $\Delta\phi$ represent the axial and azimuthal coherence scales, respectively, and generally depend on the frequency ω. Assuming statistical independence of ϵ and ϕ', the intensity (variance of pressure) on the surface is

$$< pp^* > (x,\phi) \; =< \epsilon\epsilon^* > \left| p_0\left(\frac{x}{L_x}\right)\right|^2 \int_{-\pi}^{\pi} \left|\mathcal{D}\left(\frac{\phi-\phi'}{\Delta\phi}\right)\right|^2 f(\phi')d\phi' \tag{27}$$

where $<>$ denotes the ensemble average and * denotes the complex conjugate (the expectation of the product of functions of two orthogonal random variables is addressed in Papoulis[33]). For axisymmetric jets the density is uniform, $f(\phi) = 1/(2\pi)$. For asymmetric jets, the density is lower on the "quiet" side and higher on the "loud" side. For $|\mathcal{D}(\phi/\Delta\phi)|^2$ sufficiently narrow so that it acts on the pdf like a Dirac delta function,

$$< pp^* > (x,\phi) \; \approx A < \epsilon\epsilon^* > \left| p_0\left(\frac{x}{L_x}\right)\right|^2 \; f(\phi) \tag{28}$$

with

$$A \; = \; \int_{-\pi}^{\pi} \left|\mathcal{D}\left(\frac{\phi}{\Delta\phi}\right)\right|^2 d\phi$$

Under this condition the pdf $f(\phi)$ describes the azimuthal variation of the intensity on the wavepacket surface. Obviously the approximation of Eq. 28 holds for frequencies large enough that the coherence falls off rapidly with azimuthal separation.

It can be readily derived that the far-field pressure created by the event of Eq. 26 is[30]

$$p_{far}(R,\theta,\phi-\phi',\alpha) \; = \; -i\epsilon\frac{L_x}{\pi R}\; e^{i\alpha R}\; \widehat{p}_0\left(\alpha L_x\cos\theta\right) \sum_{m=-\infty}^{\infty} \frac{g_m e^{-i|m|\frac{\pi}{2}}}{H^{(1)}_{|m|}\left(\alpha y_0 \sin\theta\right)} e^{im(\phi-\phi')} \tag{29}$$

where $\widehat{p}_0$ is the Fourier transform of p_0, $H^{(1)}_m$ is the Hankel function of the first kind of order m, and g_m are the coefficients of the complex Fourier-series expansion of $\mathcal{D}(\phi)$:

$$\begin{aligned} \mathcal{D}(\phi) &= \sum_{m=-\infty}^{\infty} g_m e^{im\phi} \\ g_m &= \frac{1}{2\pi}\int_{-\pi}^{\pi} \mathcal{D}(\phi)e^{-im\phi}d\phi \end{aligned} \tag{30}$$

The intensity (autospectrum) in the far field is

$$S_{PP}(R,\theta,\phi,\alpha) \; =< \epsilon\epsilon^* > \frac{L_x^2}{\pi^2 R^2}\left|\widehat{p}_0\left(\alpha L_x\cos\theta\right)\right|^2 \int_{-\pi}^{\pi} \Gamma(\phi-\phi',\theta,\alpha)f(\phi')d\phi' \tag{31}$$

with

$$\Gamma(\phi,\theta,\alpha) \; = \; \left| \sum_{m=-\infty}^{\infty} \frac{g_m e^{-i|m|\frac{\pi}{2}}}{H^{(1)}_{|m|}\left(\alpha y_0\sin\theta\right)} e^{im\phi}\right|^2 \tag{32}$$

In Eq. 31 the function Γ defines the azimuthal field of influence of a source at ϕ' on a far-field observer at spherical coordinates (R,θ,ϕ).

The azimuthal function $\mathcal{D}$ is modeled here as a Gaussian:

$$\mathcal{D}\left(\frac{\phi}{\Delta\phi}\right) = \exp\left[-\left(\frac{\phi}{\Delta\phi}\right)^2\right] \tag{33}$$

Figure 5 shows the field of influence $\Gamma(\phi)$ for a disturbance with azimuthal width $\Delta\phi = 30°$ located at $\phi' = 0$. For low Strouhal number the far-field influence is broad and affects significantly the sound field for all azimuthal angles. With increasing frequency, the influence becomes more confined to angles near $\phi = 0°$. Figure 6 presents a more general perspective by plotting contour maps of Γ versus ϕ and Sr for different $\Delta\phi$. It is seen that the influence at low and moderate frequencies is fairly insensitive to the width $\Delta\phi$.

A few remarks on the validity of this approach are in order. The model is based on a narrow $\Delta\phi$ representing weak azimuthal coherence of the pressure on the near-field cylinder. There is experimental evidence that the azimuthal correlation of the velocity fluctuations in the jet is indeed very weak, approximately 10° at $x/D = 1$ and 45° at $x/D = 10$.[34] Near-field pressure measurements also show weak azimuthal correlations;[35,36] however, those measurements were made at $r/D = 1.5$ to 2 and are thus influenced by the azimuthal spreading of the disturbance. Nevertheless, for high-speed jets the azimuthal correlation is weak, even at low Strouhal number.[36]

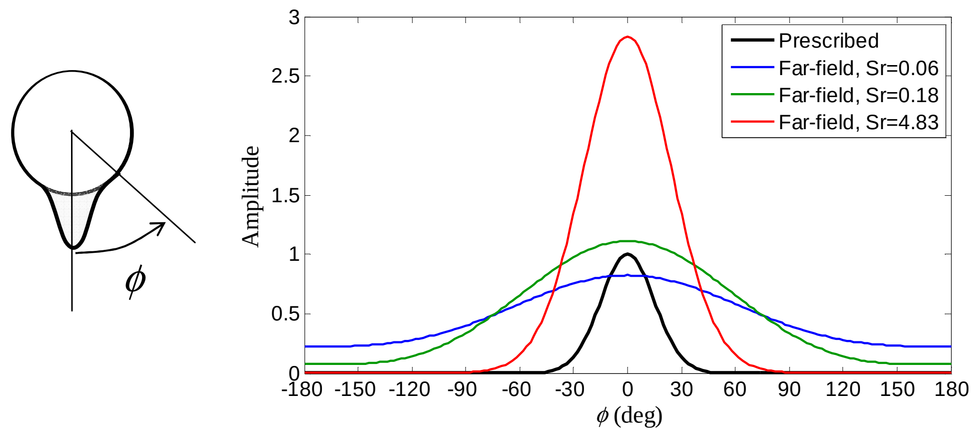

Figure 5. Azimuthal influence Γ in the far field of a Gaussian disturbance with $\Delta\phi = 30°$. Polar angle $\theta = 40°$.

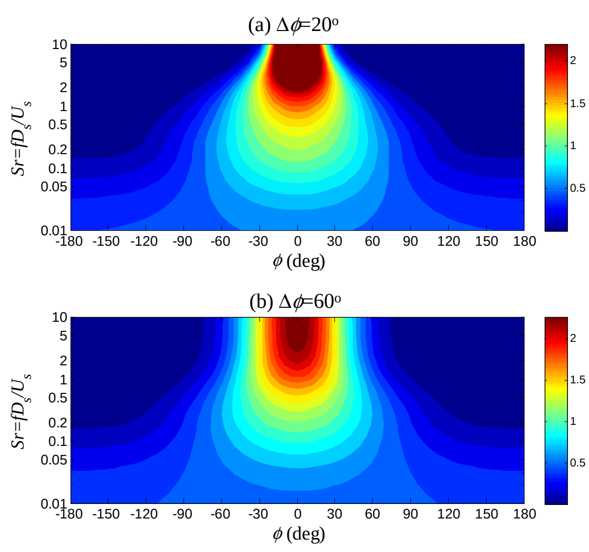

Figure 6. Contour maps of azimuthal influence function Γ versus Strouhal number and azimuthal angle. (a) $\Delta\phi = 20°$; (b) $\Delta\phi = 60°$.

C. Refraction Through the Jet Flow

Before attempting to apply the azimuthal spreading of Eq. 32 to the acoustic analogy formulation, we need to address the effects of refraction through the jet flow. The model of the previous section does not consider the transmission of a pressure wave, generated by the isolated event, through the jet and its emergence from the "inert" portion of the jet column. If the transmission generates a considerable perturbation on the other side of the jet, the entire thesis of the model is in question as the presumed isolated event would no longer be isolated. We may argue that the weak azimuthal correlation of the near-field pressure is proof in itself that such transmission is weak, at least in the context of peak noise. However, it is important to develop a model that explains the physical reasons why this may be the case.

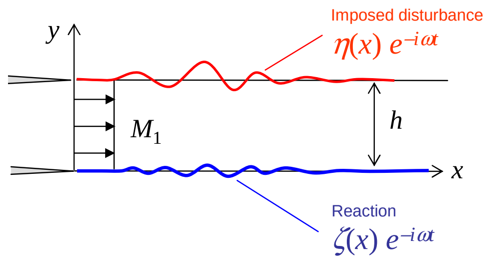

Figure 7. Two dimensional jet setup for studying transmission of a disturbance through the jet.

To address this issue at an elementary level we study the 2D problem of sound transmission through an inviscid, parallel jet column of height h, Mach number M_1, density ρ_1, and speed of sound a_1. The surrounding medium has conditions M_∞, ρ_∞ and a_∞. The setup is illustrated in Fig. 7. We consider a harmonic problem wherein we perturb the upper interface of the jet with shape $\eta(x)e^{-i\omega t}$ and calculate the response of the lower interface $\zeta(x)e^{-i\omega t}$. The lower interface is taken to be passive in the sense that we do not consider its own (Kelvin-Helmholtz) instability. A similar problem was addressed by Papamoschou[37] in a model for attenuation of Mach waves through a subsonic layer. On expanding all the variables in their axial Fourier transforms, e.g.,

$$\varphi(x,y) \;=\; \frac{1}{2\pi}\int_{-\infty}^{\infty} \widehat{\varphi}(k_x,y)e^{ik_x x}dk_x \tag{34}$$

we show readily that the acoustic potential is governed by the Helmholtz equation

$$\begin{aligned} \left(\frac{\partial^2}{\partial y^2} \;+\; K^2\right)\widehat{\varphi} \;&=\; 0 \\ K^2 \;&= \kappa^2 - k_x^2 \\ \kappa &= \frac{\omega}{a} - Mk_x \end{aligned} \tag{35}$$

Here K is a transformed lateral wavenumber that encapsulates the effects of convection (Mach number M) on acoustic propagation. The general solution is

$$\widehat{\varphi} \;= \widehat{A}(k_x)e^{iKy} \;+\; \widehat{B}(k_x)e^{-iKy} \tag{36}$$

The solution is radiative for $K^2 \geq 0$ and exponentially decaying for $K^2 < 0$. More insight into the role of K is gained by writing it as

$$K \;=\; |k_x|\left[\left(\frac{\omega}{k_x a} - M\right)^2 - 1\right]^{1/2} \tag{37}$$

The term inside the parentheses is the phase Mach number of a wave at k_x relative to its surrounding medium. When the phase Mach number is subsonic K is imaginary and the solution decays exponentially. When the phase Mach number is supersonic K is real and the solution radiates. The generation of *acoustic* (versus hydrodynamic) pressure is associated with supersonic phase Mach numbers. It is obvious that the flow Mach number M reduces the range of *positive* axial wavenumbers over which radiation occurs. In the problems of interest here, the wave energy is concentrated almost entirely in positive axial wavenumbers.

The physics of propagation are further illustrated in Fig. 8. The energy of the disturbance is concentrated at axial wavenumber $k_x = \omega/U_c$; it is taken to have a supersonic convective velocity ($U_c > a_\infty$) although the argument is equally valid for subsonic U_c. Equation 37 provides the range of wavenumbers that radiate in a particular medium. Assuming that the ambient air is static ($M_\infty = 0$), the range of outward radiating wavenumbers is $-\omega/a_\infty < k_x < \omega/a_\infty$. The range of inward radiating wavenumbers (into the jet core) is $-(\omega/a_1)/(1 - M_1) < k_x < (\omega/a_\infty)/(1 + M_1)$. So the range of inward radiating wavenumbers is much narrower than the outward range because of the Mach number effect and because the jet flow is hotter. This means that only a very small fraction of the energy contained in the disturbance $\eta(x)$ radiates inward; most of the energy directed inward decays exponentially.

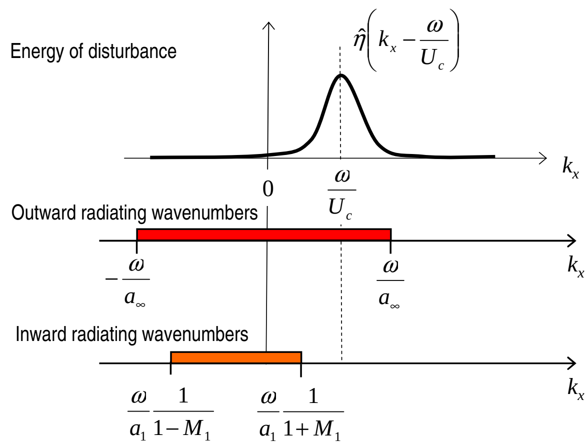

Figure 8. Radiating wavenumbers for the problem of Fig. 7.

To proceed with the solution we apply the kinematic boundary condition on the upper and lower interfaces, and pressure equality on the lower interface (the upper interface does *not* represent a physical solution, so it supports a pressure discontinuity). The reader is referred to Ref. 37 for the basic steps. We obtain a relation between the upper and lower interfaces:

$$\widehat{\zeta} = \begin{cases} \widehat{\eta}\ [\cos(|K_1|h) + Z\sin(|K_1|h)]^{-1}, & K_1^2 > 0 \\ \widehat{\eta}\ [\cosh(|K_1|h) + Z\sinh(|K_1|h)]^{-1}, & K_1^2 \le 0 \end{cases} \tag{38}$$

with

$$Z = \frac{\gamma_\infty \kappa_\infty^2 K_1}{\gamma_1 \kappa_1^2 K_\infty} \tag{39}$$

The pressure field emitted outward is

$$\begin{aligned} \widehat{p}_{+\infty}(k_x, y) &= i\rho_\infty a_\infty^2 \frac{\kappa_\infty^2}{K_\infty} e^{-iK_\infty(y-h)}\ \widehat{\eta} \\ \widehat{p}_{-\infty}(k_x, y) &= -i\rho_\infty a_\infty^2 \frac{\kappa_\infty^2}{K_\infty} e^{iK_\infty y}\ \widehat{\zeta} \end{aligned} \tag{40}$$

for the upward ($y \ge h$) and lower ($y \le 0$) regions.

Considering a static ambient medium ($M_\infty = 0$), the acoustic (radiated) pressure field on and above the upper side of the jet is

$$p_{+\infty}(x, y) = \frac{i\rho_\infty \omega^2}{2\pi} \int_{-\alpha}^{\alpha} \frac{\exp\left[i(k_x x - \sqrt{\alpha^2 - k_x^2}\ (y - h)\right]}{\sqrt{\alpha^2 - k_x^2}}\ \widehat{\eta}(k_x) dk_x \tag{41}$$

where once again $\alpha = \omega/a_\infty$. The transonic singularity in the denominator is removed via the coordinate transformation $k_x = \alpha \sin\chi$, yielding

$$p_{+\infty}(x, y) = \frac{i\rho_\infty \omega^2}{2\pi} \int_{-\pi}^{\pi} \exp\left[i\alpha_\infty(x\sin\chi - (y - h)\cos\chi)\right]\ \widehat{\eta}(\alpha_\infty \sin\chi) d\chi \tag{42}$$

Similarly, for the lower part of the domain,

$$p_{-\infty}(x,y) \;=\; -\frac{i\rho_\infty \omega^2}{2\pi}\int_{-\pi}^{\pi} \exp\left[i\alpha_\infty (x\sin\chi + y\cos\chi)\right]\;\widehat{\zeta}(\alpha_\infty \sin\chi)d\chi \tag{43}$$

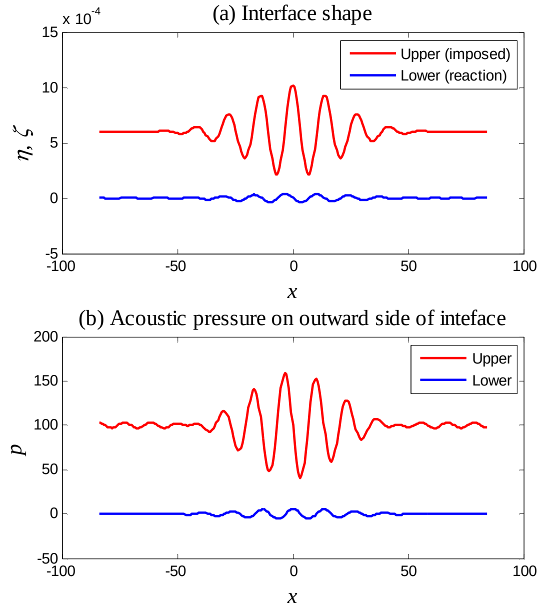

Figure 9. Transmission of a wavepacket-type disturbance through a 2D jet with $M_1 = 1.03$, $U_1 = 600$ m/s, Sr =0.05. (a)Interfaces $\eta(x)$ and $\zeta(x)$; (b) acoustic pressure fields on the outward sides of the interfaces.

We now treat an interface having a wavepacket-type shape

$$\eta(x) \;=\; \exp\left[-\left(\frac{x}{L_x}\right)^2 + i\frac{\omega}{U_c}x\right] \tag{44}$$

It describes a sinusoidal perturbation propagating downstream with convective velocity U_c and having a Gaussian amplitude modulation with axial scale L_x. Its Fourier transform is

$$\widehat{\eta}(k_x) \;=\; L_x \exp\left[-\frac{1}{4}\left(k_x - \frac{\omega}{U_c}\right)^2 L_x^2\right] \tag{45}$$

and indicates that the energy of the disturbance is concentrated around $k_x = \omega/U_c$. The conditions in the 2D jet column are the same as those of the primary stream of this study, to be presented in Section V.A: $M_1 = 1.03$, $a_1 = 590$ m/s, $U_1 = M_1 a_1 = 600$ m/s. The ambient environment is at $a_\infty = 345$ m/s, $M_\infty = 0$. The convective velocity is taken to be $U_c = 0.7U_1$, consistent with prevailing models and in accord with RANS results to be reviewed in Section V.B.2. Figure 8 plots the interfaces and pressure fields at the interfaces for Strouhal number $Sr = 2\pi\omega h/U_1 = 0.05$ and $L_x = 1.5\omega/(2\pi U_c)$ (1.5 times the instability wavelength). The curves for the lower and upper results are offset for clarity. The acoustic field generated by the upper disturbance is strongly attenuated by the jet flow, resulting in a very small perturbation of the lower surface and a very weak pressure field on the lower surface. With increasing Strouhal number the lower perturbation becomes several orders of magnitude weaker than the upper perturbation.

The physical reason for the rapid attenuation of the disturbance through the layer is that the phase Mach number inside the jet is low subsonic for the energetic part of the wavenumber spectrum (see Eq. 37, Fig. 8, and related discussion). In other words, there is very little radiation within the jet column. Extension of the above analysis to axisymmetric or 3D jets is non-trivial and will be the subject of future studies. However, the same physical mechanisms are expected to hold: the refraction of a wavepacket-type disturbance through the jet will be so weak as to be overwhelmed by the azimuthal influence function introduced in Section III.B.

In summary, we expect the azimuthal influence function Γ to adequately capture the azimuthal spreading of a disturbance that simulates the large-scale structures in the jet.

The previous arguments may not hold when the observer is situated at large angle to the jet axis. At large angles, the wavepacket radiation is very weak so the intensity of the refracted sound may become comparable to the emission intensity. This issue will be the subject of future studies as we examine the extension of this model to angles off the direction of peak emission.

D. Application to Acoustic Analogy Problem

In this section we modify the acoustic analogy model to include the azimuthal directivity concept developed in the last two subsection. Before presenting this modification, it is important to realize that azimuthal directivity concept is inherently valid in the shear-layer portion of the jet. It is not expected to hold past the end of the potential core, where large-scale structures comprise the entire flow field. For this reason, the acoustic analogy model will be used without any modification for the region past the end of the potential core (approximately $x/D_s > 6$). We note, however, that extending the modification past the end of the potential core had minimal impact on the results.

There are obvious analogies of the surface-source integral of Eq. 31 to the volume-source integral obtained by combining Eqs. 12 and 16. Equation 12 can be expressed in cylindrical polar coordinates $\mathbf{y} = (x, y, \phi)$:

$$S_{PP}(\mathbf{x}, \omega) = \frac{\omega^4}{16\pi^2 a_\infty^4 R^2} \int_0^\infty \int_0^\infty \int_{-\pi}^{\pi} H\left[(x, y, \phi'),\ \boldsymbol{\alpha},\ \omega\right] d\phi' y dy dx \tag{46}$$

As noted earlier, this integral cannot capture the azimuthal influence of the source H. In analogy with the surface-source treatment of the previous section, the azimuthal variation of H is connected to the pdf $f(\phi)$ times a proportionality factor $G(\alpha)$ that absorbs A and $< \epsilon\epsilon^* >$ in Eq. 28. Accordingly Eq. 46 is modified with an azimuthal influence factor $G(\alpha)\Gamma(\phi, \theta, \alpha)$ as follows:

$$S_{PP}(\mathbf{x}, \omega) = \frac{\omega^4\ G(\alpha)}{16\pi^2 a_\infty^4 R^2} \int_0^\infty \int_0^\infty \int_{-\pi}^{\pi} H\left[(x, y, \phi'),\ \boldsymbol{\alpha},\ \omega\right]\ \Gamma(\phi - \phi', \theta, \alpha) d\phi' y dy dx \tag{47}$$

For an axisymmetric jet H is independent of ϕ' and Eq. 47 should give exactly the same result as Eq. 46. This means

$$G(\alpha) = \frac{2\pi}{\int_{-\pi}^{\pi} \Gamma(\phi, \theta, \alpha) d\phi}$$

and therefore

$$S_{PP}(\mathbf{x}, \omega) = \frac{1}{8\pi a_\infty^4 R^2} \frac{\omega^4}{\int_{-\pi}^{\pi} \Gamma(\phi, \theta, \alpha) d\phi} \int_0^\infty \int_0^\infty \int_{-\pi}^{\pi} H\left[(x, y, \phi'),\ \alpha\mathbf{x}/R,\ \omega\right]\ \Gamma(\phi - \phi', \theta, \alpha) d\phi' y dy dx \tag{48}$$

More generally, we write

$$S_{PP}(\mathbf{x}, \omega) = \frac{1}{8\pi a_\infty^4 R^2} \frac{\omega^4}{\int_{-\pi}^{\pi} \Gamma(\phi, \theta(\mathbf{x}), \alpha) d\phi} \int_{\mathcal{V}} H\left(\mathbf{y},\ \alpha\mathbf{x}/R,\ \omega\right)\ \Gamma\left(\phi(\mathbf{x}) - \phi(\mathbf{y}), \theta(\mathbf{x}), \alpha\right) d^3\mathbf{y} \tag{49}$$

where $\phi(\mathbf{y})$ is the azimuthal angle of a given source volume element; and $\theta(\mathbf{x})$ and $\phi(\mathbf{x})$ are the polar and azimuthal coordinates of the far-field observer, respectively. The azimuthal influence function Γ is given by Eq. 32.

The selection of coordinate system for defining the azimuthal angle ϕ is critical. The nozzle axis is a poor choice as the fan flow deflectors impart a downward tilt to the jet plume and deform the cross-sectional shape. In previous work we used the centroid of the mass flux to define the "center" of the jet at a given axial location.[3] Further study has shown that the centroid based on the momentum flux gives better results, with the centroid consistently coinciding with the location of minimum turbulent kinetic energy near the end of the potential core. Accordingly, we define the centroid as

$$Y_c(x) = \frac{\int_{A(x)} \overline{\rho}\ \overline{u}^2 Y dA}{\int_{A(x)} \overline{\rho}\ \overline{u}^2 dA} \tag{50}$$

where Y is the transverse coordinate on the symmetry plane and $A(x)$ is the cross-sectional area of the plume at a given axial location x. Once the centroid is computed, the $Y-$coordinates of all the data are reset to a new frame (by subtracting $Y_c(x)$) where $Y = 0$ is the centroid location.

IV. Parameterization of the Source

In Section II we discussed the formulation of a model for the far-field pressure autospectrum of the axisymmetric jet in terms of parameters that govern the space-time correlation of the source. Here we describe the procedure for determining those parameters so that we match the baseline (axisymmetric) sound pressure level spectra.

A. Source Parameters

As noted in Section II.C, for a given polar angle θ the prediction of the far-field autospectrum is governed by the scale coefficients C_1, C_2, C_4 and the shape coefficients $\beta_1, \beta_2, \beta_4$. The amplitude of the spectrum is an additional parameter; however, its determination is trivial in the context of this study. The coefficients form a parameter vector

$$V_k(\theta) \ = [C_1(\theta),\ C_2(\theta),\ C_4(\theta),\ \beta_1(\theta),\ \beta_2(\theta),\ \beta_4(\theta)] \tag{51}$$

The far-field spectrum, obtained by combining Eqs. 12 and 20, can be written in the form

$$S_{PP}(\mathbf{x},\omega) \ = \ S_{PP}(\ V_k(\theta(\mathbf{x})),\ \mathbf{x},\ \omega\ ) \tag{52}$$

B. Determination of Parameters for Baseline Jet

We seek to match the experimental *baseline* spectra. It is convenient to work with the Sound Pressure Level (SPL) spectrum, in units of decibels. The modeled SPL spectrum is

$$\mathrm{SPL}_{\mathrm{mod}}(\ V_k(\theta(\mathbf{x})),\ \mathbf{x},\ \omega\ ) \ = \ 10\log_{10}\left[\frac{S_{PP}(\ V_k(\theta(\mathbf{x})),\ \mathbf{x},\ \omega\ )}{S_{ref}}\right] \tag{53}$$

with $S_{ref} = 4\times10^{-10}$ Pa^2. The experimental SPL spectrum is $\mathrm{SPL}_{\mathrm{exp}}(\mathbf{x},\omega)$. We facilitate the optimization by normalizing the spectrum by its maximum value. Equivalently, in decibels we subtract the maximum value. The normalization removes the effect of distance R, so the normalized spectrum depends only on the parameter vector and the observer polar angle (recall that the baseline jet is axisymmetric, so there is no azimuthal variation of the spectrum). The normalized modeled and experimental SPL spectra are:

$$\begin{aligned}\mathrm{SPL}^*_{\mathrm{mod}}(V_k(\theta),\omega) \ &= \mathrm{SPL}_{\mathrm{mod}}(V_k(\theta),R,\omega) - \mathrm{SPL}_{\mathrm{mod,max}}(V_k(\theta),R)\\ \mathrm{SPL}^*_{\mathrm{exp}}(\theta,\omega) \ &= \mathrm{SPL}_{\mathrm{exp}}(\theta,R,\omega) - \mathrm{SPL}_{\mathrm{exp,max}}(\theta,R)\end{aligned} \tag{54}$$

This normalization removes the amplitude as a variable, so we are concerned only with matching the shape of the spectra.

For a given jet flow, the experimental SPL is known at discrete frequencies ω_j, $j = 1,..,J$. We construct a cost function based on the variance between the modeled and experimental SPL at a specific polar angle θ.

$$F(V_k) = \frac{1}{J}\sum_{j=1}^{J}\left[\mathrm{SPL}^*_{\mathrm{mod}}(V_k,\omega_j) - \mathrm{SPL}^*_{\mathrm{exp}}(\omega_j)\right]^2 \tag{55}$$

We then seek determination of V_k that minimizes the cost function. The minimization process of Eq. 55 uses the Restarted Conjugate Gradient method of Shanno and Phua[38] (ACM TOM Algorithm 500).

C. Application to Jets with Fan Flow Deflection

Upon a reasonable match of the baseline modeled and experimental spectra, the parameter vector V_k is known for each polar angle of interest. This parameter vector is now applied to the jets with fan flow deflection, using Eq. 49. The amplitude of the modeled spectrum is restored by adding $\mathrm{SPL}_{\mathrm{exp,max}}$ of the baseline spectrum, which can be considered as an additional parameter in the problem:

$$\mathrm{SPL}_{\mathrm{mod}}(V_k(\theta),\theta,\phi,R,\omega) \ = \mathrm{SPL}^*_{\mathrm{mod}}(V_k(\theta),\theta,\phi,\omega) + \mathrm{SPL}_{\mathrm{exp,max}}(\theta,R) \tag{56}$$

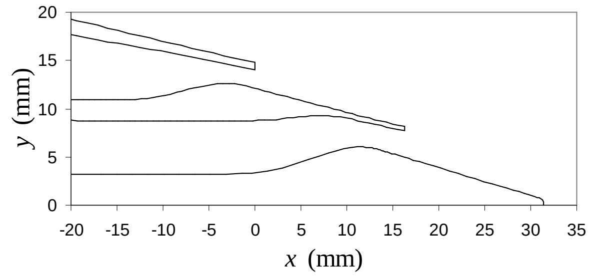

Figure 10. Nozzle coordinates.

V. Application Fields

So far we have described a methodology for the acoustic prediction of symmetric and asymmetric jets and the parameterization of the problem based the far-field sound of the baseline (symmetric) jet. Again, we are interested in predicting the noise *reduction* from a known baseline. In this section we describe the experimental and computational data for the jets to which this methodology will be applied. The jets have been the subject of previous publications,[3] so this section summarizes only the information pertinent to the present study.

A. Experimental

The experiment utilized a separate-flow coaxial plug nozzle designed for bypass ratio BPR=2.7. The fan exit diameter was $D_s = 28.1$ mm and the fan exit height was 1.8 mm. The nozzle coordinates are plotted in Fig. 10. The acoustic tests were performed with the primary flow at fully-expanded velocity $U_p = 600$ m/s and fully-expanded Mach number $M_p = 1.03$. The corresponding values for the secondary flow were $U_s = 400$ m/s and $M_s = 1.15$. These conditions were enabled using cold helium-air mixture jets, which have been shown to match very well the acoustics of hot air jets. The Reynolds number of the jet, based on fan diameter, was 0.92×10^6.

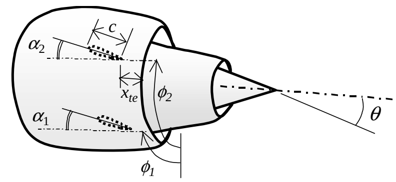

Figure 11. Geometric parameters of deflector vanes.

Fan flow deflection was achieved through the use of internal airfoil-shaped vanes that spanned the width of the annulus of the fan nozzle. Figure 11 illustrates the geometric parameters of the vanes. The vanes were micro-machined from high-strength polycarbonate material. The vane cross sections encompassed symmetric and asymmetric airfoils with NACA 0012, 4412 and 7514 sections. The base and tip of each vane were shaped to conform to the geometry of the fan and core ducts at the exact location where the vane was attached. The vane chord length was 3 mm and the vane trailing edge was situated at 2 mm upstream of the nozzle exit. Nozzles were tested with both single-pair (2V) and two-pair (4V) vane configurations at various azimuth angles and angles of attack. Table 2 lists the geometric parameters of the deflectors.

Aeroacoustic tests were conducted in U.C. Irvines Jet Aeroacoustics Facility, a subscale facility (approximately 1/50th of full scale for the tests in question) that uses helium-air mixtures for replicating the exhaust velocity and density of hot jets. Jet noise was recorded by a far-field microphone array consisting of eight 3.2-mm condenser microphones (Bruel & Kjaer, Model 4138) arranged on a circular arc centered at the vicinity of the nozzle exit. This study encompassed the azimuth angles $\phi = 0^\circ$ (downward) and $\phi = 0^\circ$ (sideline). Data from the microphone array were processed into lossless narrowband sound pressure level. Figure 12 shows selected spectra for jet 4Va with comparison to the Base jet. For angles near the angle of peak emission $\theta = 40°$ the spectrum reduces substantially at moderate and high frequency. For larger angles the spectrum remains the same or slightly increases. More experimental results will be shown in the later sections of this paper.

Table 1. Nozzle configurations

Configuration	Aifoil	α_1, deg	ϕ_1, deg	α_2, deg	ϕ_2, deg
Baseline	–	–	–	–	–
2Va	0012	7.5	90	–	–
2Vb	0012	7.5	150	–	–
2Vc	7514	4.0	120	–	–
4Va	7514	4.0	50	4.0	120
4Vb	0012	7.5	90	7.5	150
4Vc	4412	7.5	90	4.0	150
4Vd	7514	4.0	50	4.0	90

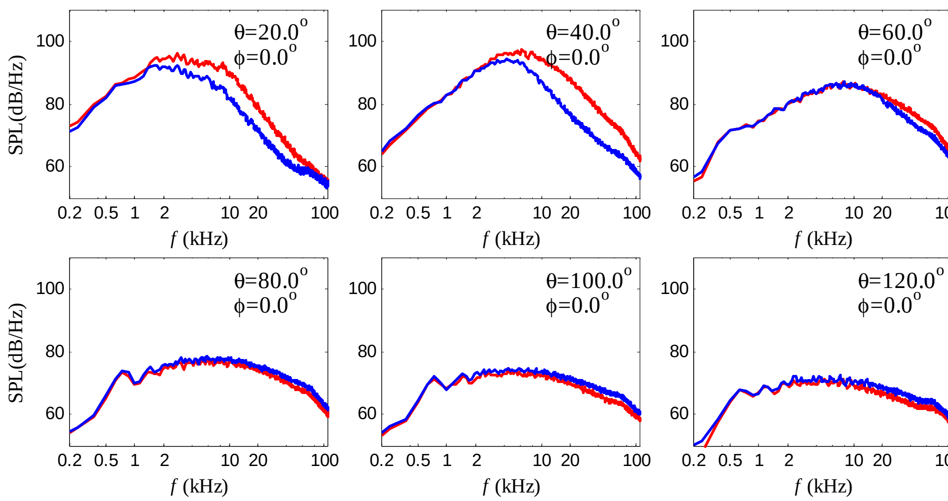

Figure 12. Narrowband far-field spectra for jet 4Va (blue) with comparison to Base jet (red) for various polar angles θ. Azimuthal direction $\phi = 0°$ (downward).

B. Computational

1. Code

The computational fluid dynamics code used is known as PARCAE.[39] It solves the unsteady three-dimensional Reynolds-averaged Navier-Stokes (RANS) equations on structured multiblock grids using a cell-centered finite-volume method with artificial dissipation as proposed by Jameson et al.[40] Information exchange for flow computation on multiblock grids using multiple CPUs is implemented through the MPI (Message Passing Interface) protocol. The RANS equations were solved using the Shear Stress Transport (SST) turbulence model of Menter.[41] The SST model combines the advantages of the k-Ω and k-ϵ turbulence models for both wall-bounded and free-stream flows.

Multi-block grids were generated using ICEM-CFD for each vane configuration. As all the configurations were symmetric around the meridional plane, only one half of the nozzle was modeled to save computational expense. In order to simulate the jet flow, the grid extended about $3.8D_s$ radially outward from the nozzle centerline and over $20D_s$ downstream of the nozzle. The grids were clustered all along the wall boundaries. The base nozzle grid had 3.7 million grid points. The two-vane and four-vane configurations had 4.9 million and 5.8 million grid points, respectively. For all the grids, the minimum $y+$ of the first grid point from the wall was less than 1. The average $y+$ values were about 3. Wall functions were not required. The grids were divided into multi-blocks to implement parallelization on multiprocessors computers to reduce convergence time. Convergence was determined once the average residuals of both the continuity and momentum equations decreased at least three orders of magnitude and the changes of the residuals between successive iterations reduced to the order of 0.01%. Comparison with experimental mean-flow profiles showed excellent agreement, as illustrated by the example of Fig. 13. Additional comparisons can be found in Ref. 3.

The optimization scheme of this study would have been prohibitively expensive using the full computational grid of several million points. Instead, the computational size was reduced significantly by dismissing points with very low value of turbulent kinetic energy. Threshold sensitivity studies indicated that a grid size of approximately 50,000 was more than adequate for the parameterization. Once the parameter vector was determined, the spectrum was computed using a lower-threshold grid of about 100,000 points.

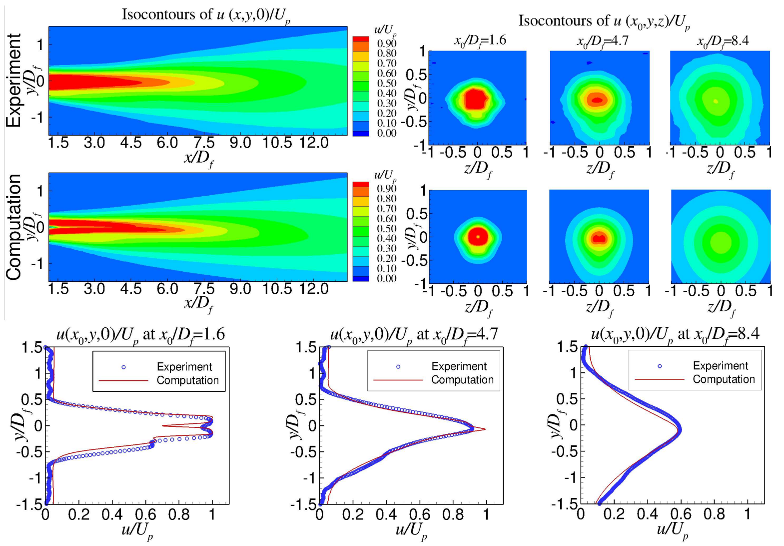

Figure 13. Comparison of experimental and computational mean-velocity results for jet 4Va. From Ref. 3.

2. *Relevant Statistics*

We examine flow variables, statistics, and scales relevant to the acoustic analogy modeling. We comment on three representative configurations: Base, 2Va, and 4Va. Figure 14 plots contour maps of the mean axial velocity $\overline{u}$ and turbulent kinetic energy k on the symmetry plane. The thickening of the flow and downward deflection of the plume with increasing strength of the fan flow deflectors is evident. The suppression of k on the underside of the jet is moderate for 2Va and strong for 4Va. The region of zero or near-zero k in the vicinity of the axis of the nozzle is a good indication of the extent of the potential core. Note that the centroid, as defined in Eq. 50, passes exactly through the point where this region ends.

It is now instructive to examine the relevant parameters on a surface on which the turbulent kinetic energy is maximized. It is anticipated that this surface will represent the location of the strongest sources of noise. Specifically, for each x and ϕ we compute the value and radial location of the peak turbulent kinetic energy $k_{\max}$, then we calculate the values of characteristic length, frequency, and velocity scales at the $k_{\max}$ locations. In Fig. 15 we plot those variables for jet 2Va at $\phi = 0°$ (quiet side) and $\phi = 180°$ (loud side), and compare it to the Base jet. Figure 15a shows the axial distribution of $k_{\max}$. For the Base jet $k_{\max}$ peaks at $x/D_s = 5.5$ which is the end of the potential core, as is evident from Fig. 15a. For jet 2Va we note appreciable reduction of $k_{\max}$ in the downward direction ($\phi = 0°$) and moderate increase in the upward direction ($\phi = 180°$).

The turbulent length scale $k^{1/2}\Omega$, normalized by the fan diameter D_s, grows approximately linearly with axial distance, Fig. 15b. The step-wise behavior near $x/D_s = 4$ is related to the end of the secondary core and the transition of the location of $k_{\max}$ from the secondary (outer) shear layer to the primary (inner) shear layer. In other words, upstream of $x/D_s \approx 4$ the dominant noise source is in the outer shear layer and the inner shear layer is "quiet". Once the secondary core is exhausted, the inner shear layer becomes the dominant noise source. It is clear that the fan flow deflection prolongs the transition point in the downward

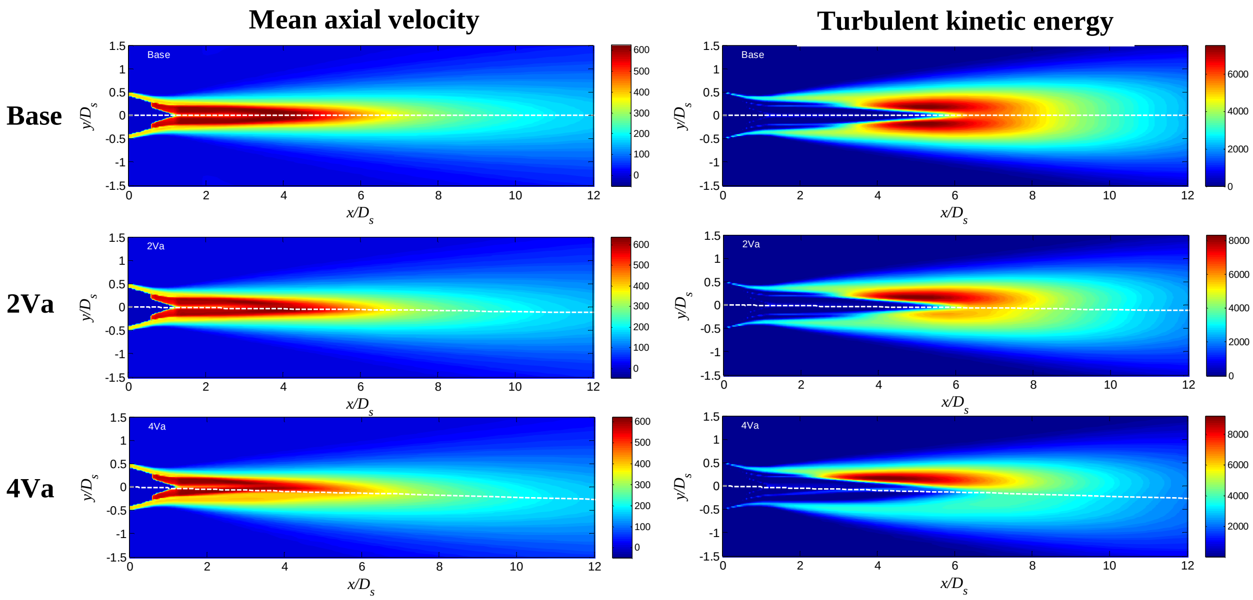

Figure 14. RANS predictions of mean axial velocity (m/s) and turbulent kinetic energy (m^2/s^2) fields for selected cases. Dashed line indicates centroid location.

direction, consistent with its intended purpose. Generally speaking, the length scale $k^{1/2}\Omega$ seems to represent adequately the physical thickness of the turbulent part of the flow, assuming the value of D_s near the end of the potential core. On the other hand, the time-based length scale $U_c\tau_*$, plotted in Fig. 15c, grows about four times faster.

The non-dimensional frequency (Strouhal) scale $\Omega D_s/(2\pi U_s)$ is plotted in Fig. 15d. It decays roughly as $1/x$ and displays a step where the secondary core ends, like the turbulent length scale in Fig. 15b. The axial distribution of convective Mach number M_c is plotted in Fig. 15e. For the Base jet, M_c stats at low value of 0.6, jumps to supersonic value of 1.18 at $x/D_s = 3$, then gradually decays with downstream distance. The initially low value is because the dominant source is the outer shear layer between the secondary stream ($U_s = 400$ m/s) and the ambient. Once the secondary core is dissipated at $x/D_s \approx 4$ the inner shear layer ($U_p = 600$ m/s) is exposed to the ambient and becomes the dominant noise source, resulting in the jump of M_c. The downstream decline is associated with the end of the potential core and the decay of the peak velocity. Jet 2Va displays similar trends, with the location of the jump delayed to $x/D_s \approx 4.5$ due to the elongation of the secondary core on the underside of the jet. There is no significant reduction in the peak value of M_c. For the Base jet, the initial value of M_c corresponds to U_c/U_s=0.52 and the peak value corresponds to U_c/U_p=0.68. Both ratios are in line with prevailing models for the convective speed in compressible shear layers.[22] The frequency dependence of the turbulent length scale is shown in Fig. 15f. For all the cases plotted the slope of this relation on the log-log plot is around -1 for non-dimensional frequencies higher then 0.01, which is in line with the expectation proposed by Morris and Zaman.[20]

Figure 16 plots the analogous information for jet 4Va. Here we see a substantial reduction of turbulent kinetic energy on the underside of the jet. Importantly, there is a sharp reduction of the convective Mach number in the downward direction, with its peak value declining from 1.18 in the Base jet to 0.82 for 4Va. For this flow we expect the noise reduction to depend on both the lower turbulent kinetic energy and the lower convective Mach number. The latter governs the efficiency with which a given volume element radiates to the far field.

The convective Mach number trends in Figs. 15 and 16 are in line with postulates of early works on fan flow deflection on the underlying physical mechanism – namely the reduction of convective Mach number of the "instability waves" (large-scale structure) responsible for the peak noise radiation.[2] Those hypotheses were based solely on experimental mean-velocity profiles and empirical models for the convective velocity. It is noteworthy that the RANS solution, which is devoid of any time-resolved information, provides results that capture this critical aspect of noise emission from a dual-stream jet.

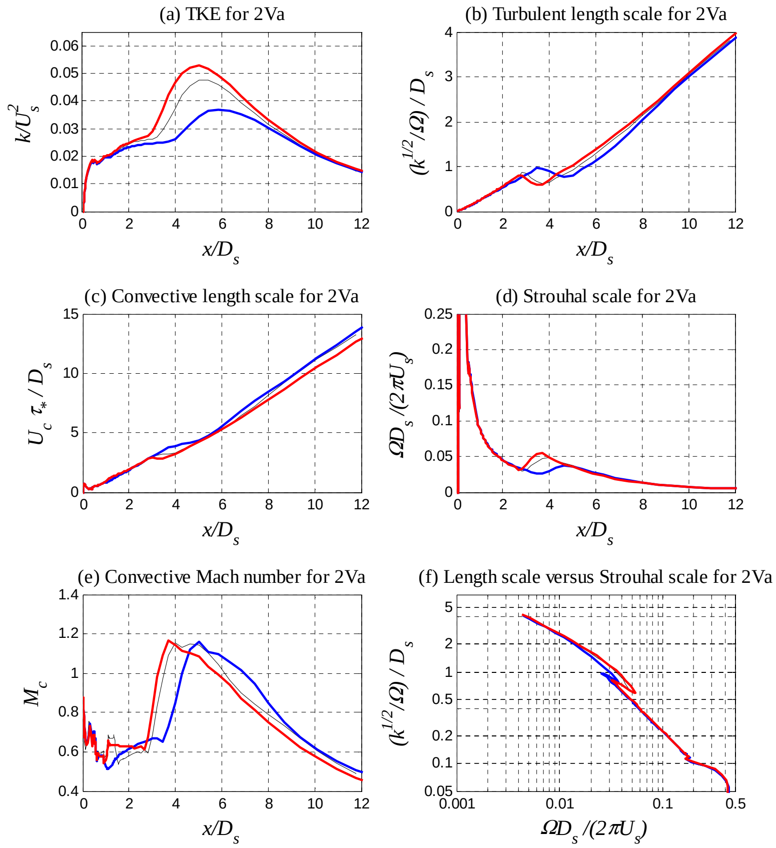

Figure 15. Characteristic scales at location of peak turbulent kinetic energy k_{max}. Jet 2Va at $\phi = 0°$ (blue) and $\phi = 180°$ (red) is compared to Base jet (black). Axial distribution of (a) k_{max}; (b) turbulent length scale; (c) time-based length scale; (d) Strouhal scale; (e) convective Mach number. (f) Frequency dependence of turbulent length scale.

VI. Results

Our study has introduced several new elements in the acoustic analogy modeling of peak noise from high-speed turbulent jets: a broader class of functions for expressing the space-time correlation; a definition of convective Mach number based on the locus of peak turbulent kinetic energy; and an azimuthal directivity formulation based on the wavepacket model of large-scale structure noise. In this section we present initial results of this modeling effort, with application to the BPR=2.7 jet reviewed in Section V.

A. Modeling of the Baseline Jet

We apply the parameterization scheme of Section III to the baseline (axisymmetric) jet. The process starts with an initial value of the parameter vector V_k of Eq. 51, typically $V_k = (1.0, 1.0, 1.0, 1.5, 1.5, 1.5)$. The conjugate gradient minimizer converged after about 10 function calls to a minimum error (square root of the cost function, Eq. 55) of about 1 dB. Each trial minimization, starting from slightly different initial values, lasted about five minutes with a set of 50,000 flow points. The trials ended with similar results for the parameter vector.

Figure 17 plots the experimental and modeled spectra, and displays the parameter vector resulting from the minimization. We note a very good match of the spectral shapes. It should be pointed out that this agreement was not possible when using the "traditional" definition of convective Mach number $M_c = \overline{u}/a_\infty$, regardless of the values of the parameter vector. This observation underscores the importance of a proper definition of M_c when modeling noise in the direction of peak emission.

The coefficients C_1, C_2, and C_4 are on the order of 0.5, which is in agreement with past studies that modeled peak jet noise.[17] Regarding the powers β_j of the stretched/compressed-exponential function, we

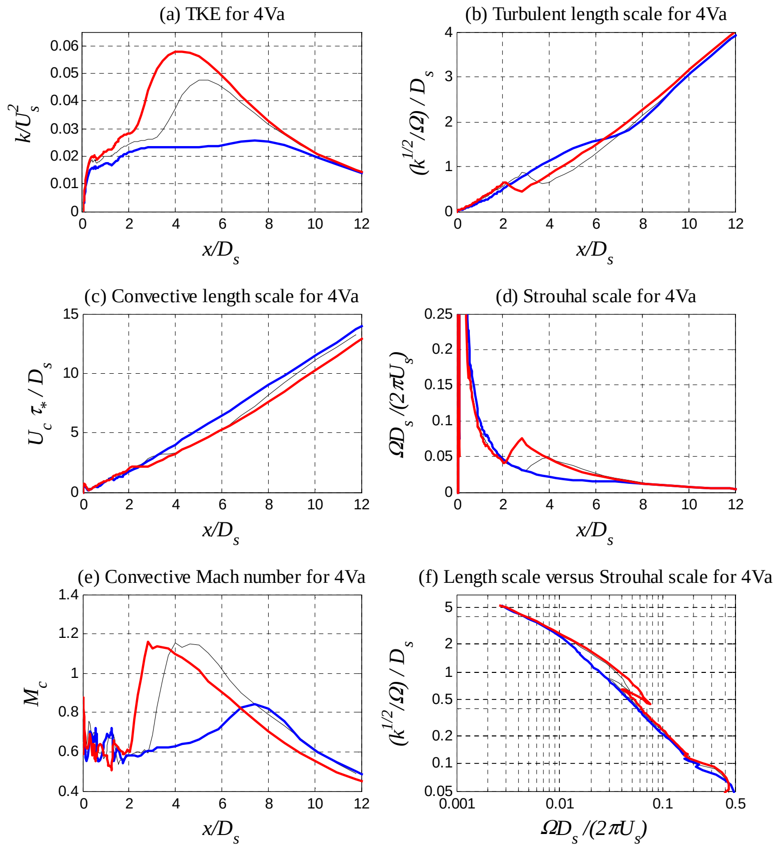

Figure 16. Characteristic scales at location of peak turbulent kinetic energy k_{max}. Jet 4Va at $\phi = 0°$ (blue) and $\phi = 180°$ (red) is compared to Base (black). Axial distribution of (a) k_{max}; (b) turbulent length scale; (c) time-based length scale; (d) Strouhal scale; (e) convective Mach number. (f) Frequency dependence of turbulent length scale.

consistently obtained $\beta_1 \sim 1$ and $\beta_2, \beta_4 \sim 1.5$. The exponential decay of the R_1 correlation in Eq. 13 is supported by experimental data showing that the correlation of the second-order moments decays exponentially with axial separation ξ_x.[14,20] The hybrid behavior of the other correlations (between exponential and Gaussian) reflects the mixed trends found for the transverse correlations and the fourth-order correlations.[14]

B. Modeling of the Deflected Jet

The parameter vector determined from previous step is now applied to all the deflected jets. In modeling the deflected jet, we have the additional variable $\Delta\phi$ which describes the azimuthal extent of an isolated disturbance (Eqs. 26, 33) and can be interpreted as the azimuthal coherence angular scale L_ϕ/y_0. As noted in Section III.B, the far-field azimuthal pattern is fairly insensitive on $\Delta\phi$. Although ideally we would set $\Delta\phi(\mathbf{y}) = L_\phi(\mathbf{y})/y_0$, this results in a very time-consuming computation as Γ in Eq. 32 needs to be evaluated for each point in the flow field. Several trials indicated that the low-frequency part of the spectrum was virtually independent of $\Delta\phi$ in the range $20° \leq \Delta\phi \leq 90°$. The high end of the spectrum did not change for $\Delta\phi \leq 40°$. Therefore, the value $\Delta\phi = 20°$ was used in evaluating the azimuthal influence function Γ in Eq. 32.

Figure 18 plots the experimental and modeled spectra for the 2V jets at azimuth observer locations $\phi = 0°$ and $\phi = 60°$ (downward and sideline directions, respectively). The spectra are compared to the Base jet. The modeled reductions are similar to the experimental reductions, with a slight under-prediction of the reductions in the sideline direction. Importantly, the model discerns which configurations among the three 2V cases are the least- and most-promising. The vane configuration of 2Vb gives poor results because the vanes are placed very close to the top of the jet and thus do little to thicken the fan flow in the sideward

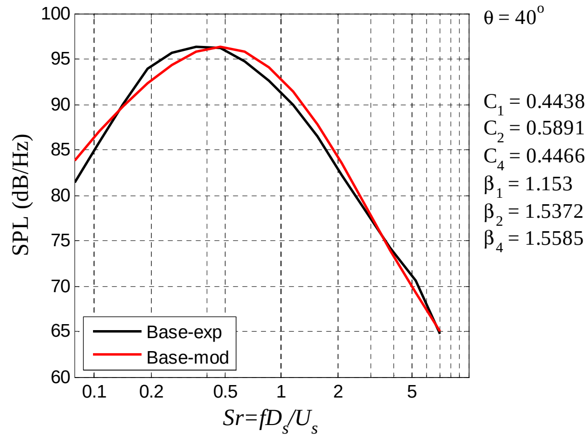

Figure 17. Parameterization of baseline (axisymmetric jet). Black line is experimental sound pressure level spectrum at $\theta = 40°$. Red line is the modeled spectrum in the same direction. The optimized parameters are displayed on the right.

and downward directions. The vanes in 2Vc are placed at 120°, an azimuthal placement that maximizes downward and sideline noise reductions. The model was able to predict both trends.

Figure 19 presents the corresponding information for the 4V jets. The model predicts the increase in noise reduction enabled by the stronger deflection of the fan flow. It does a reasonable job at medium and high frequencyes ($Sr > 1$) but it tends to over-predict the noise reduction at the peak frequency. Also, it underpredicts the sideline reductions. Overall, it gives the designer a fair assessment of the noise reduction for Sr 1 and, as in the 2V cases, provides guidance as to which cases are the most/least promising. For example, jet 4Vd has marginal sideline reduction, a trend that the model was able to capture.

VII. Examination of the Source

In this section we examine the source fields associated with the modeling of Section VI and review the validity of the major assumption underlying wavepacket model of Section III: that the azimuthal directivity of the pressure autospectrum on the near-field wavepacket surface is similar to the azimuthal directivity of the wavenumber-frequency spectrum in the far-field formulation of Eq. 12.

A. Noise Source Distribution on Symmetry Plane

We examine the distribution of the wavenumber-frequency spectrum $H(\mathbf{y}, \boldsymbol{\alpha}, \omega)$ for the Base and 4Va jets. The spectrum H represents the volumetric "source" as measured by a far-field observer at $\theta = 40°$. Figure 20 plots isocontours of H on the symmetry plane. With increasing frequency the noise source becomes confined to thin annular layers, which is consistent with our hypothesis in Section III. For the Base jet, the source location moves upstream with increasing Strouhal number but then gets fixed at $x/D_s = 3.5$ up to high Strouhal number. This invariance of source location in coaxial jets has been noted in noise-source imaging of full-scale engine exhausts[42] and in subscale tests.[43] The location of the invariance is related to the termination of the secondary core and the emergence of the primary shear layer as the dominant noise generator, In other words, it is related to the M_c trend seen in the Base curves of Figs. 15 or 16. The 4Va jet exhibits very different behavior because its shear-layer structure is altered, with the secondary core elongating on the bottom side and shrinking on the top side.

B. Near-Field Evaluation

To assess the validity of our assumption on the azimuthal pattern of pressure on the near-field cylinder in Section III, we conduct a near-field evaluation of the acoustic pressure on a cylindrical surface of radius $y = y_0 = 0.6D_s$. Figure 21 gives an impression of where the cylinder is located relative to the noise source.

The near-field evaluation requires use of the full expression for the spectrum, Eq. 9. Inserting the

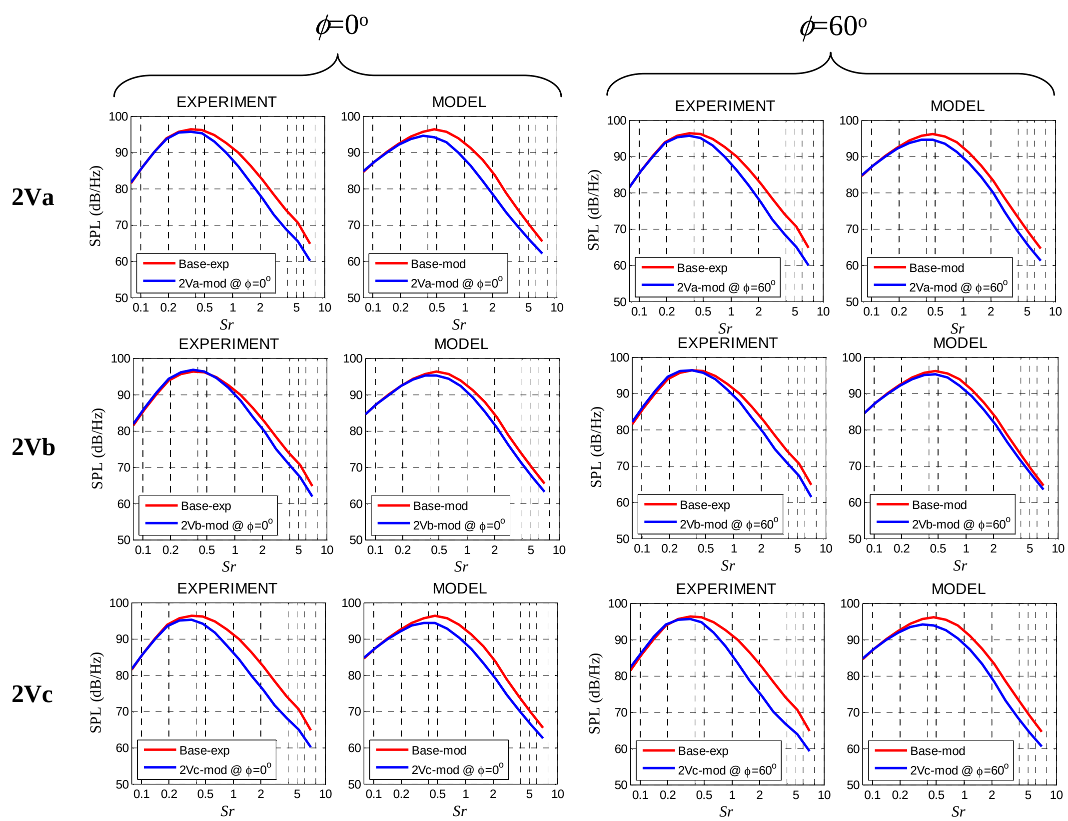

Figure 18. Experimental and modeled spectra for the 2V cases (blue curves) with comparison to the Base (red curves).

correlation form of Eq. 13 we obtain

$$S_{PP}(\mathbf{x},\omega) = \frac{\omega^4}{16\pi^2 a_\infty^5} \int_{\mathcal{V}} \int_{\mathcal{V}_\xi} \vartheta_i \vartheta_j \vartheta'_k \vartheta'_l \; A_{ijkl} \; \frac{L_x}{M_c} \; R_1\left(\frac{\xi_x}{L_\tau}\right) \; R_2\left(\frac{\xi_y}{L_y}\right) \; R_3\left(\frac{\xi_\phi}{L_\phi}\right) \; \widehat{R}_4\left(\frac{\alpha L_x}{M_c}\right) \times \exp\left\{ i \left[\alpha \left(r' - r - \frac{\xi_x}{M_c} \right) - \omega\tau \right] \right\} \; \frac{1}{rr'} \; d^3\boldsymbol{\xi} \; d^3\mathbf{y} \tag{57}$$

with $r = |\mathbf{x}-\mathbf{y}|$, $r' = |\mathbf{x}-\mathbf{y}-\boldsymbol{\xi}|$, $\vartheta_i = (x_i - y_i)/r$, $\vartheta'_i = (x_i - y_i - \xi_i)/r'$. As before, the stretched/compressed exponential $R_j(\eta) = \exp(-|\eta|^{\beta_j})$ is used as the generic correlation function. The axial, radial, and circumferential separations between points $\mathbf{y'} = (x', y', \phi')$ and $\mathbf{y} = (x, y, \phi)$ are defined as:

$$\begin{aligned} \xi_x &= x' - x \\ \xi_y &= y' - y \\ \xi_\phi &= \frac{1}{2}(y + y')(\phi' - \phi) \end{aligned} \tag{58}$$

The length, velocity, time, and A_{ijkl} scales are defined in Eqs. 21 and 22. The coefficients C_1, C_2, C_4, β_1, β_2, $\beta_3 = \beta_2$, and β_4 are those determined by the parameterization process of Section III. Proper use of Eq. 57 in the very near field requires thresholding of the source to ensure that the field points on the cylinder surface are outside the source region. Otherwise, singularities occur and the use of the free-field Green's function, manifested in the $1/(rr')$ term, is invalid. Thresholding was applied to the source "magnitude" $A_{ijkl}L_x/M_c$. Values less than 5% of the peak value (at a given frequency) were set to zero. The term A_{ijkl} was set to either $\rho^2 u_*^4$ (self noise) or $\rho^2 \overline{u}^2 u_*^2$ (shear noise). Both formulations gave practically identical results. In the example that follows the truncated noise source was confined to within $y/D_s = 0.5$ and the field points were placed at $y/D_s = 0.6$.

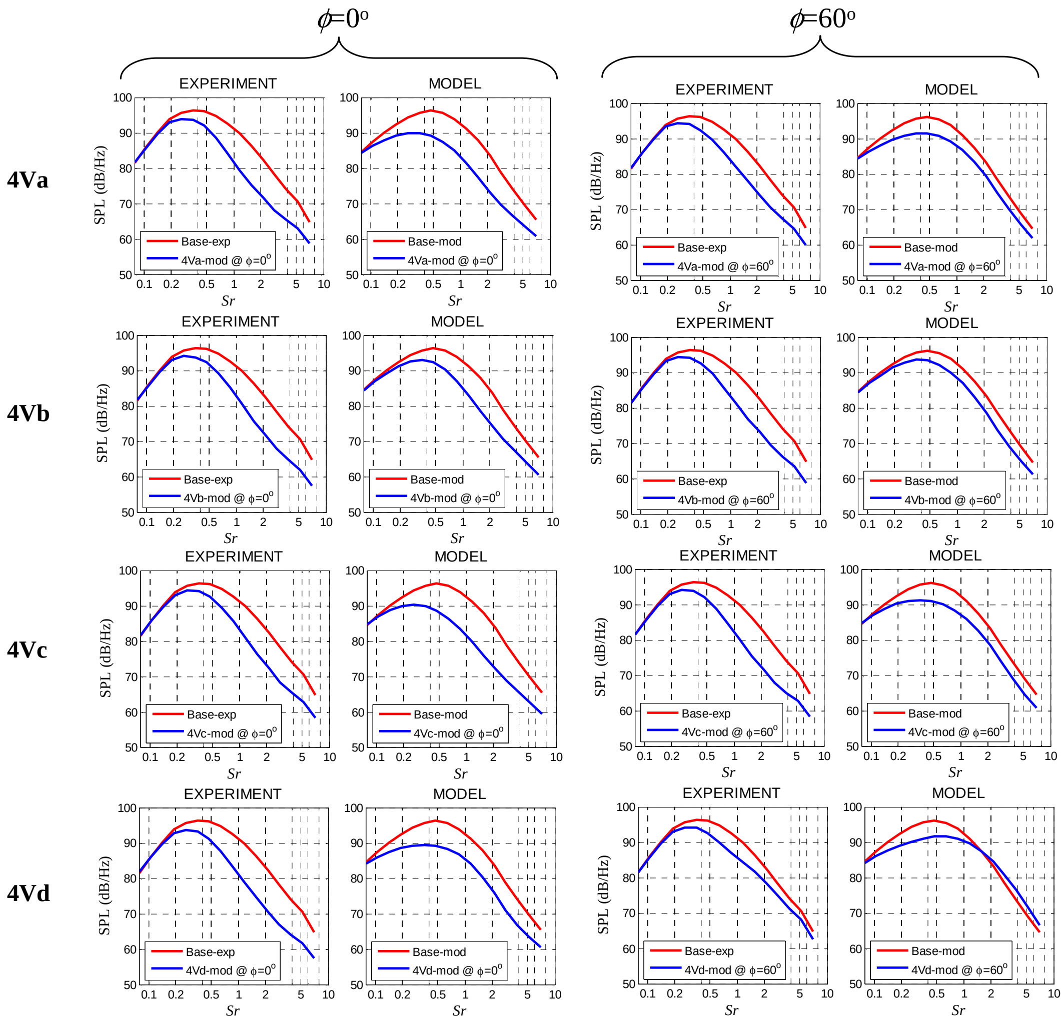

Figure 19. Experimental and modeled spectra for the 4V cases (blue curves) with comparison to the Base (red curves).

The computation of Eq. 57 is obviously very demanding, requiring $(N^2 + N)/2$ operation for each field point, where N is the number of grid points in the source volume. Significant savings are realized by conducting the integrations within the neighbourhood of each field point. Here the neighourhood was a sphere of radius $1D_s$, resulting in $N \approx 15{,}000$. Figure 22 plots contour maps of the azimuthal directivities on the $x-\phi$ plane for the peak value of the wavenumber-frequency spectrum H and the pressure autospectrum S_{PP} on the cylindrical surface. The contour maps are shown for the 4Va jet at $Sr = 0.86$. We note that H and S_{PP} have similar axial and azimuthal patterns, with the pattern of S_{PP} slightly spread out shifted to the right. The shift is consistent with the downstream direction of the peak emission (recall that S_{PP} is the autospectrum of the acoustic pressure.) Results of the other cases are similar. The comparison of Fig. 20 provides qualitative, if not quantitative, support for the coupling between the Lighthill source and the wavepacket model of Section III. Additional points of scrutiny may include the separable form of the turbulent event of Eq. 26, which leads to the azimuthal spreading being independent of the axial shape. Although more elaborate models may be used, it should be remembered that the azimuthal spreading is quite insensitive on initial conditions. The “forgiving” nature of this aspect of wavepacket emission may not warrant the complexity of a non-separable model.

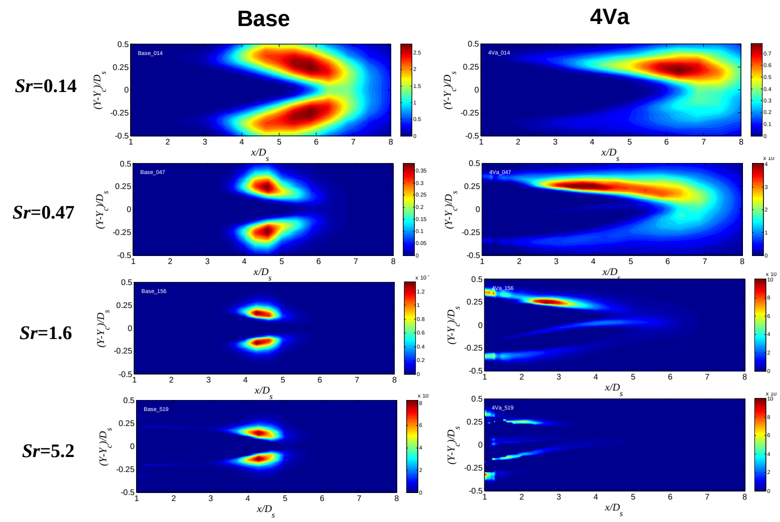

Figure 20. Distribution of wavenumber-frequency spectrum H on symmetry plane.

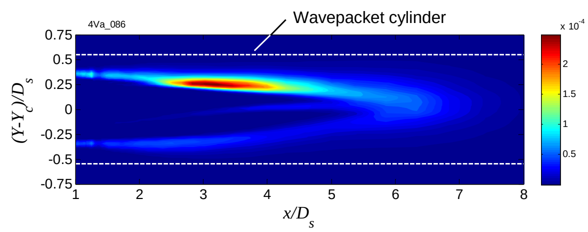

Figure 21. Distribution of wavenumber-frequency spectrum H at on symmetry plane at $Sr = 0.86$. Dashed lines indicate the location of the wavepacket cylinder.

VIII. Conclusions

Our study was motivated by the need of an *engineering* tool to predict the spectral changes caused by fan flow deflection in dual-stream, high-speed jets. Specifically, we wanted to evaluate whether a RANS solution, coupled to a Lighthill-based acoustic analogy model, could be up to this task. The underlying philosophy was to take the baseline spectrum as known, use it to calibrate the acoustic analogy model, then predict the deflected jet based on this calibration. The principal features of our approach were:

- Use of Lighthill-based acoustic analogy, versus other approaches that include refraction but are much more complex and computationally expensive. Consistent with the nature of large-scale noise, we argue that refraction should not play a significant role on outward radiation. A simple model for the inward radiation shows that it is very weak because the disturbances are intrinsically subsonic with respect to the jet flow.

- Implementation of a wavepacket model for the prediction of the azimuthal directivity. This approach is compatible with our interest in the radiation from large-scale structures. The wavepacket model includes a stochastic model for the surface pressure distribution, which is then linked to the volumetric "source" of the acoustic analogy model.

- Use of a generalized space-time correlation model wherein the statistics are described in a fixed frame and the correlation shapes are flexible (not necessarily exponential or Gaussian). The shape parameters and correlation coefficients comprise a six-dimensional parameter vector that defines the acoustic emission for a given RANS solution.

- Definition of a convective Mach number based on the mean axial velocity at the locus of peak turbulent kinetic energy.

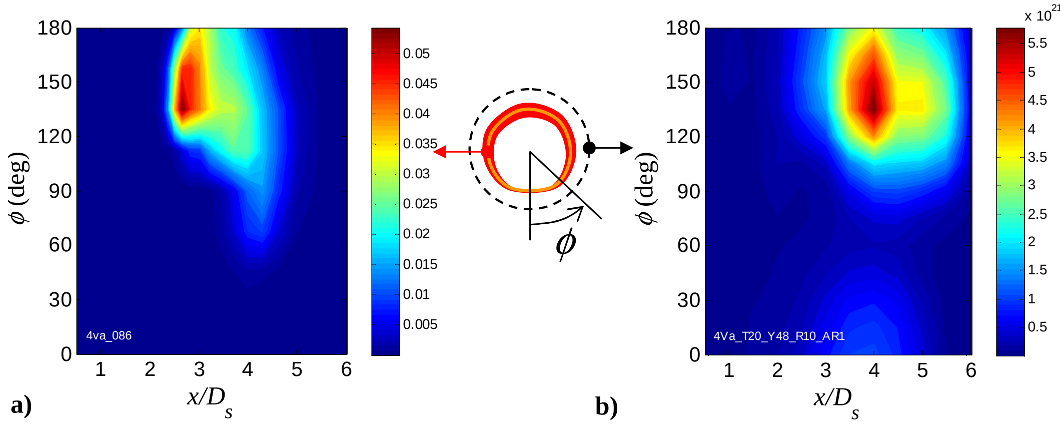

Figure 22. Distribution of source versus axial distance and azimnutal angle for 4Va jet at $Sr = 0.86$. a) Peak value of wavenumber-frequency spectrum H. b) Variance of pressure on near-field wavepacket cylinder.

- Parameterization of the baseline (axisymmetric) jet and determination of the parameter vector using the conjugate-gradient method.

The model was able to capture the main noise reduction trends measured in the experiments. Perhaps more importantly, the model provided physical insight into the mechanism of noise reduction: it is reduction of turbulent kinetic energy combined with a reduction in convective Mach number. Proper modeling of the convective Mach number was crucial. Simply setting $M_c = \overline{u}/a_\infty$ resulted in failure to faithfully reproduce the baseline spectrum and to predict with any level of satisfaction the reductions caused by the fan flow deflection. This failure is apparent in Fig. 22 which shows the prediction for the Base and 4Va jets using $M_c = \overline{u}/a_\infty$. Although the spectrum of the Base jet is reconstructed with some fidelity, the spectrum of the 4Va jet is predicted poorly. In contrast, the M_c model used here (Eq. 25) captures the salient aspects of noise emission from a dual-stream jet and leads to reasonable predictions of the baseline and deflected jets. It is thus remarkable that the RANS computation, which is devoid of any time-resolved information, can provide a parameter that is linked to the radiation of instability waves.

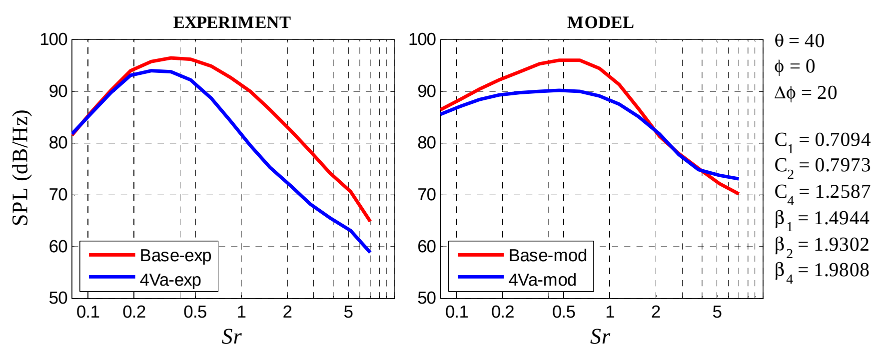

Figure 23. Spectral predictions for the Base and 4Va spectra using $M_c = \overline{u}/a_\infty$. Compare with Fig. 19.

The flexibility afforded by the stretched/compressed-exponential formulation of the correlation shapes was crucial. It should be no surprise that the correlations are not purely exponential or Gaussian. On the other hand, the far-field solution was insensitive on whether the magnitude of the correlation was modeled as "shear noise" or "self noise." Further, the solution was quite insensitive on the assumed azimuthal coherence scale used in the azimuthal directivity formulation of Section III, as long as the scale was narrow enough, i.e., less than about 45°.

Acknowledgments

The experimental and RANS components of this project were sponsored by NASA Cooperative Agreement NNX07AC62A, monitored by Dr. K.B.M.Q. Zaman. We thank Dr. Juntao Xiong for preparing the RANS data in a form usable for acoustic analogy modeling. The first author acknowledges discussions with Dr. Hävard Vold of ATA Engineering, Inc., on the formulation of the random event used in Section III.B.

References

[1]Brown, C., Bridges, J., and Henderson, B., "Offset-Stream Technology Test - Summary of Results," AIAA 2007-3664, January 2007.

[2]Papamoschou, D., "New Method for Jet Noise Suppression in Turbofan Engines," *AIAA Journal*, Vol. 42, No. 11, 2004, pp. 2245–2253.

[3]Xiong, J., Nielsen, P., Liu, F., and Papamoschou, D., "Computation of High-Speed Coaxial Jets with Fan Flow Deflection," *AIAA Journal*, Vol. 48, No. 10, 2010, pp. 2249–2262.

[4]Lighthill, M., "On Sound Generated Aerodynamically: I. General Theory," *Proceedings of the Royal Society of London*, Vol. 211, 1952, pp. 564–587.

[5]Morris, P. J. and Farassat, F., "Acoustic Analogy and Alternative Theories for Jet Noise Prediction," *AIAA Journal*, Vol. 40, No. 4, 2002, pp. 671–680.

[6]Harper-Bourne, M., "Jet Near-Field Noise of Combat Aircraft," AIAA 1999-1838, May 1999.

[7]Lilley, G., "On the Noise from Jets," *Noise Mechanisms, CP-131 AGARD*, 1974, pp. 13.1–13.12.

[8]Morris, P. and Boluriaan, S., "The Prediction of Jet Noise from CFD Data," AIAA 2004-2977, May 2004.

[9]Goldstein, M. and Leib, S., "The Aeroacoustic of Slowly Diverging Supersonic Jets," *Journal of Fluid Mechanics*, Vol. 600, 2008, pp. 291–337.

[10]Mani, R., "The Influence of Jet Flow on Jet Noise. Part 1. The Noise of Unheated Jets," *Journal of Fluid Mechanics*, Vol. 73, No. 4, 1976, pp. 753–778.

[11]Tam, C. and Auriault, L., "Mean Flow Refraction Effects on Sound Radiated from Localized Sources in a Jet," *Journal of Fluid Mechanics*, Vol. 370, 1998, pp. 149–174.

[12]Lighthill, M., "On Sound Generated Aerodynamically. II. Turbulence as a Source of Sound," *Proceedings of the Royal Society of London*, Vol. 222, 1954, pp. 1–32.

[13]Harper-Bourne, M., "Predicting the Jet Near-Field Noise of Combat Aircraft," AIAA 2002-2424, June 2002.

[14]Harper-Bourne, M., "Jet Noise Turbulence Measurements," AIAA 2003-3214, May 2003.

[15]Bassetti, A., Morfey, C., and Harper-Bourne, M., "Impact of the Source-Correlation Model in Jet-Noise Prediction by Acoustic Analogy," AIAA 2007-3604, May 2007.

[16]Tam, C. and Auriault, L., "Jet Mixing Noise from Fine-Scale Turbulence," *AIAA Journal*, Vol. 37, pp. 145–153.

[17]Karabasov, S., Afsar, M., Hynes, T., Dowling, A., McMullan, W., Pokora, C., Page, G., and Guirk, J., "Jet Noise: Acoustic Analogy Informed by Large Eddy Simulation," *AIAA Journal*, Vol. 48, No. 7, 2010, pp. 1312–1325.

[18]Hamm, P., Helbing, J., and Bredenbeck, J., "Stretched Versus Compressed Exponential Kinetics in α-Helix Folding," *Chemical Physics*, Vol. 323, No. 1, 2006, pp. 54–65.

[19]Ribner, H., "Quadrupole Correlations Governing the Pattern of Jet Noise," *Journal of Fluid Mechanics*, Vol. 38, 1969, pp. 1–24.

[20]Morris, P. and Zaman, K., "Velocity Measurements in Jets with Application to Jet Noise," *Journal of Sound and Vibration*, Vol. 329, 2010, pp. 394–414.

[21]Brown, G. and Roshko, A., "On Density Effects and Large Structure in Turbulent Mixing Layers," *Journal of Fluid Mechanics*, Vol. 64, 1974, pp. 775–816.

[22]Murakami, E. and Papamoschou, D., "Eddy Convection in Supersonic Coaxial Jets," *AIAA Journal*, Vol. 38, No. 4, 2000, pp. 628–635.

[23]Thurow, B., Naibo, J., Kim, J.-H., Lempert, W., and Samimy, M., "Issues with Measurements of the Convective Velocity of Large-Scale Structures in the Compressible Shear Layer of a Free Jet," *Physics of Fluids*, Vol. 20, 2008, pp. 066101–1–15.

[24]Lyrintzis, A. and Mankbadi, R., "Prediction of the Far-Field Jet Noise Using Kirchhoff's Formulation," *AIAA Journal*, Vol. 34, Feb. 1996, pp. 413–416.

[25]Tam, C. and Burton, D., "Sound Generation by the Instability Waves of Supersonic Flows. Part 2. Axisymmetric Jets," *Journal of Fluid Mechanics*, Vol. 138, 1984, pp. 273–295.

[26]Crighton, D. and Huerre, P., "Shear-Layer Pressure Fluctuations and Superdirective Acoustic Sources," *Journal of Fluid Mechanics*, Vol. 220, 1990, pp. 355–368.

[27]Avital, E., Sandham, N., and Luo, K., "Mach Wave Radiation by Mixing Layers. Part I: Analysis of the Sound Field," *Theoretical and Computational Fluid Dynamics*, Vol. 12, 1998, pp. 73–90.

[28]Morris, P., "A Note on Noise Generation by Large Scale Turbulent Structures in Subsonic and Supersonic Jets," *International Journal of Aeroacoustics*, Vol. 8, No. 4, 2009, pp. 301–316.

[29]Reba, R., Narayanan, S., and Colonius, T., "Wave-Packet Models for Large-Scale Mixing Noise," *International Journal of Aeroacoustics*, Vol. 9, 2010, pp. 533–558.

[30]Papamoschou, D., "Wavepacket Modeling of the Jet Noise Source," AIAA 2011-2835, June 2011.

[31]Freund, J., Lele, S., and Moin, P., "Calculation of the Radiated Sound Field Using an Open Kirchoff Surface," *AIAA Journal*, Vol. 34, No. 5, 1996, pp. 909–916.

[32]Vold, H., Shah, P., Morris, P., Du, Y., and Papamoschou, D., "Axisymmetry and Azimuthal Modes in Jet Noise," 18th AIAA/CEAS Aeroacoustics Conference, June 2012.

[33]Papoulis, A., *Probability, Random Variables, and Stochastic Processes*, McGraw-Hill, New York, 1965, p. 211.

[34]Sreenivasan, K., “The Azimuthal Correlations of Velocity and Temperature Fluctuations in an Axisymmetric Jet,” *Physics of Fluids*, Vol. 27, No. 4, 1983, pp. 867–875.

[35]Fuchs, H., “Space Correlations of the Fluctuating Pressure in Subsonic Turbulent Jets,” *Journal of Sound and Vibration*, Vol. 23, No. 1, 1972, pp. 77–99.

[36]Ukeiley, L. and Ponton, M., “On the Near Field Pressure of a Transonic Axisymmetric Jet,” *AIAA Journal*, Vol. 40, 2002, pp. 1735–1744.

[37]Papamoschou, D., “Linear Model for Mach Wave Suppression in a Dual-Stream Jet,” AIAA 2000-2062, June 2000.

[38]Shanno, D. F. and Phua, K. H., “Minimization of Unconstrained Multivariate Functions,” *ACM Transactions on Mathematical Software*, Vol. 6, No. 4, 1976, pp. 618–622.

[39]Papamoschou, D., X. J. and Liu, F., “Aerodynamics of Fan Flow Deflectors for Jet Noise Suppression,” *Journal of Propulsion and Power*, Vol. 24, No. 3, 2008, pp. 437–445.

[40]Jameson, A., Schmidt, W., and Turkel, E., “Numerical Solutions of the Euler Equations by Finite Volume Methods Using Runge-Kutta Time Stepping Schemes,” AIAA 1981-1259, January 1981.

[41]Menter, F., “Two-Equation Eddy-Viscosity Turbulence Models for Engineering Applications,” *AIAA Journal*, Vol. 32, No. 8, 1994, pp. 1598–1605.

[42]Brusniak, L., Underbrink, L., and Nesbitt, E., “Phase Array Measurements of Full-Scale Exhaust Noise,” AIAA 2007-3612, May 2007.

[43]Mayoral, S. and Papamoschou, D., “Effects of Source Redistribution on Jet Noise Shielding,” AIAA 2010-0652, Jan. 2010.